

Yassine Hammoud¹, Youssef Allali², Abderrahim Saadane³

High-Resolution Lithology Detection Using Sentinel-2A, ALOS PRISM L1B Images, and Support-Vector Machines in Tagragra d’Akka Inlier of Western Anti-Atlas, Morocco


Abstract: Geological mapping faces substantial challenges due to inaccessible terrains, labor-intensive field methods, and potential interpretative errors. This study proposes an innovative approach that leverages automatic lithology classification using multispectral Sentinel-2A (10 m) and high-resolution panchromatic ALOS PRISM L1B (2.5 m) images. Applied to the Tagragra d’Akka inlier of the Anti-Atlas region, the methodology enhances spatial resolution through pansharpening, followed by unsupervised segmentation. The segmented images are classified using support vector machines (SVMs) (supervised learning algorithms) to distinguish the lithological units. Achieving an 86% overall accuracy and an 84% kappa coefficient, the approach demonstrated robust performance and surpassed conventional techniques. The integration of machine learning and remote sensing offers a promising frontier for geological mapping – particularly in regions like the Tagragra d’Akka inlier. This study marks a significant advancement in automating lithological mapping, with implications for geological research, resource management, and hazard assessment. Automated techniques in geological cartography significantly enhance mapping accuracy and efficiency. Future studies should explore additional data sources and machine-learning algorithms to refine lithological classification and validate these methods across diverse geological settings.

Keywords: SVM, Sentinel-2A, ALOS PRISM L1B, lithological mapping, Tagragra d’Akka


Received: March 8, 2024; accepted: January 10, 2025

2025 Author(s). This is an open-access publication, which can be used, distributed, and reproduced in any medium according to the Creative Commons CC-BY 4.0 License


¹ Mohammed V University, Faculty of Sciences, Center of Water, Natural Resources, Environment, and Sustainable Development (CERNE2D), Rabat, Morocco, email: yassine.hammoud@um5r.ac.ma (corresponding author),

 <https://orcid.org/0009-0000-8193-7425>

² Mohammed V University, Faculty of Sciences, Center of Water, Natural Resources, Environment, and Sustainable Development (CERNE2D), Rabat, Morocco, email: youssefallalix@gmail.com,

 <https://orcid.org/0000-0003-4840-8462>

³ Mohammed V University, Faculty of Sciences, Center of Water, Natural Resources, Environment, and Sustainable Development (CERNE2D), Rabat, Morocco, email: a.saadane@um5r.ac.ma,

 <https://orcid.org/0009-0000-9431-4470>

1. Introduction

Historically, classical geological mapping has relied heavily on surveyed geological cross-sections and in-field observations, inevitably leading to vulnerability to human errors. The prevalence of traditional manual methods in this process made mapping susceptible to inaccuracies, subsequently influencing the accuracy of the produced maps [1, 2].

The challenges of geological mapping are compounded by the presence of hard-to-reach areas, such as rugged terrains or dense vegetation covers [2]; these hinder geologists from conducting in-depth studies and collecting comprehensive data. These areas become sources of uncertainty and potential errors in the produced geological maps. Furthermore, the subjective nature of geological surveys further complicates mapping efforts, as different geologists may interpret and document features differently based on their individual perspectives, experiences, and expertise. This subjectivity introduces variability into the collected data, leading to discrepancies in identifying lithological extensions, boundaries, and structural details.

On another level, spectral imagery emerges as a promising solution for overcoming the limitations that are associated with precision, cost, time, and logistics constraints, which are inherent in traditional in-field geological mapping across extensive regions [3–5].

Moreover, the combination of machine learning and remote sensing has proven to be important in many applications that require massive amounts of spectral and spatial data, which are crucial for rapid information extraction. Machine learning relies on algorithms that are implemented through computer systems, computer vision, and deep-learning methods to systematically collect and identify features in a given environment.

Various machine-learning algorithms such as artificial neural networks (ANNs), support vector machines (SVMs), self-organizing maps (SOMs), decision trees (DTs), random forests (RFs), case-based reasoning (CBR), neuro-fuzzy systems (NF), genetic algorithms (GA), and multivariate adaptive regression splines (MARS) [6–14], have demonstrated their efficiency in significantly enhancing geospatial analyses. These algorithms contribute to tasks such as object classification, the identification of temporal changes, data fusion, cloud removal, geometric correction, and spectral analysis from satellite or aerial images [15].

The integration of remote sensing and machine-learning algorithms in geoscience contributes widely to the accuracy or improvement of geological mapping, particularly focusing on handling large data sets and extracting the finest lithological classes while respecting the complex nature of geological information [5].

The evolution of geological mapping has been significantly driven by advances in remote-sensing technologies [16–18], marking a transformative era in lithological mapping. Remote sensing provides a comprehensive and integrated lateral analysis of the relationships among various geological structures [2]. The use of high-resolution

multispectral data coupled with sophisticated digital image-processing capabilities such as object-based image analysis (OBIA) has greatly expanded the potential of remote sensing [19]. This improvement has facilitated the precise delineation of lithological contacts and geological structures with high precision [2, 20].

Spectral data that is collected from spaceborne sensors (primarily, widely accessible images like Landsat [5 TM, 7 ETM+, 8 OLI, and 9], ASTER, and Sentinel-2 [19]), have found applications that have extended the delineations of the structures and discriminations of rock and soil types [21–24], facilitated mineral-resource exploration (locating economic mineral deposits, identifying oil reservoirs, and detecting water resources) [25–32], and aided in understanding phenomena such as geological disasters [33].

This study is the first to exploit multispectral images from Sentinel-2A, together with the high-resolution ALOS PRISM L1B (2.5 m) panchromatic images for lithology detection. This combination offers exceptional data quality, opening up new perspectives for more-precise and -detailed geological exploration. By integrating remote sensing and machine learning, this research actively contributes to the development of lithology detection on an unprecedentedly detailed scale. These advancements offer considerable potential for natural-resource management, environmental planning, and informed decision-making in the field of geology.

Numerous studies have been conducted in the field of supervised lithological classification, each applying specific algorithms such as support vector machines [34–37], random forests (RFs) [38, 39], boosting trees [40–42], artificial neural networks (ANNs) [43–45], etc. Among these, SVM is the most popular algorithm for lithology identification and has been extensively studied. For example, Al-Anazi and Gates [34] proposed an SVM-classification formulation with a feature-selection technique based on fuzzy theory. Their results showed that the performance of the SVM-based method was superior to that of discriminant analysis and probabilistic NN. In 2014, Salehi and Honarvar [46] proposed a model that combined a least-squares support vector machine and coupled simulated annealing to predict lithology. In a study by Sebtosheikh and Salehi [35], an SVM classifier was used to predict lithology from inverted seismic data and petrophysical logs [47].

To address the current limitations in lithological mapping, the primary objectives of this study were as follows: (1) to enhance lithological-detection accuracy by using a combined SVM and remote-sensing approach; (2) to evaluate the effectiveness of pansharpened Sentinel-2A and ALOS PRISM L1B images for fine-scale lithological discrimination; and (3) to contribute to a more detailed and precise geological-exploration framework.

2. Materials and Methods

Figure 1 illustrates the methodology applied and the steps followed in presented study.

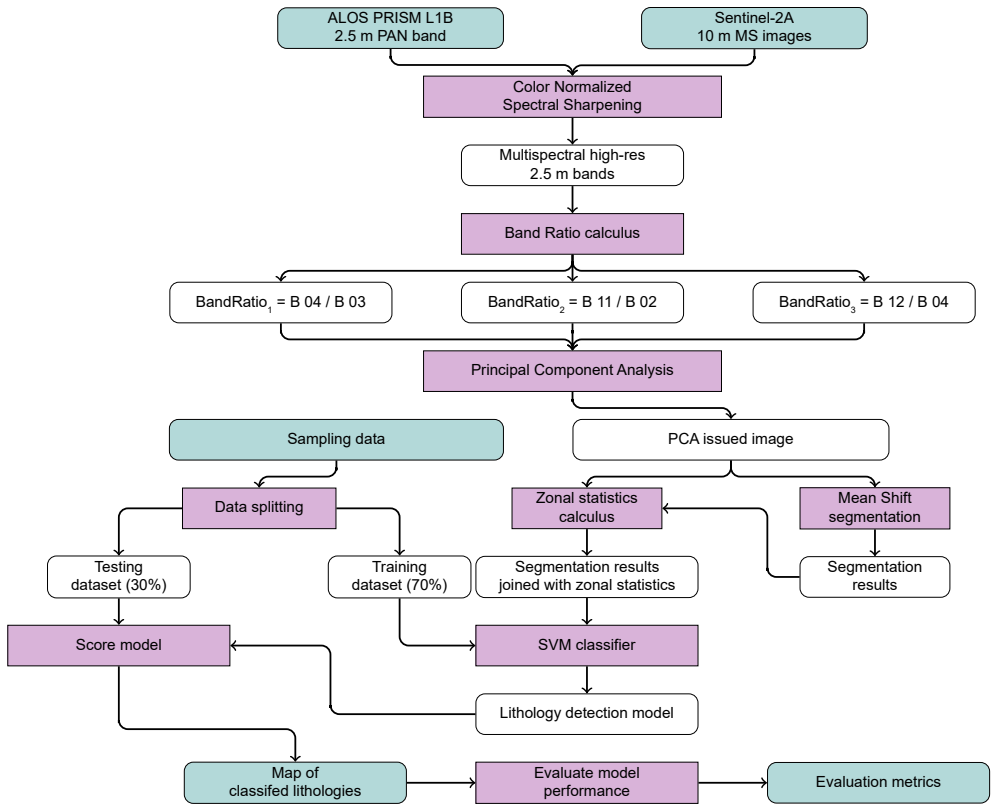


Fig. 1. Lithology-detection model-flow diagram

2.1. Study Region

Geographical Setting

The Tagragra d’Akka inlier is a unique geological structure that is located in southwestern Morocco in the Western Anti-Atlas mountain range (as shown in Figure 2). Dating back to the Paleoproterozoic era, it is situated between the Tata and Tiznit Provinces – approximately 260 km southeast of Agadir. This inlier is characterized by the presence of a set of metamorphic and igneous rocks that are exposed at the surface that date back to the Paleoproterozoic era; this provides an opportunity to study their compositions and structures [48–50].

Located at an average altitude of 933 m, the inlier features a relief that is characterized by peaks and passes that range between 900 and 1318 m as well as mountains and valleys. This barren region experiences an arid Saharan climate, resulting in high temperatures throughout the year and limited precipitation (not exceeding 100 mm per year). This low rainfall contributes to limited availability to water – both on the surface and in the groundwater [51].

From a scientific perspective, the Tagragra d’Akka inlier holds crucial importance as a privileged window for studying the formation of the Anti-Atlas Mountain range, thereby deepening the understanding of the geological processes behind this mountainous structure. As a repository of notable mineral resources (including gold and copper deposits), it also substantially contributes to advancing knowledge about the genesis and exploitation of these mineral deposits. Lastly, the inlier serves as a conducive environment for experimenting with innovative technologies such as remote sensing due to the distinctive features of its terrain (marked by the absence of vegetation and limited alteration). This opens the door to significant progress in the field of geological research.

Figure 2 illustrates the geographical setting of the study area.

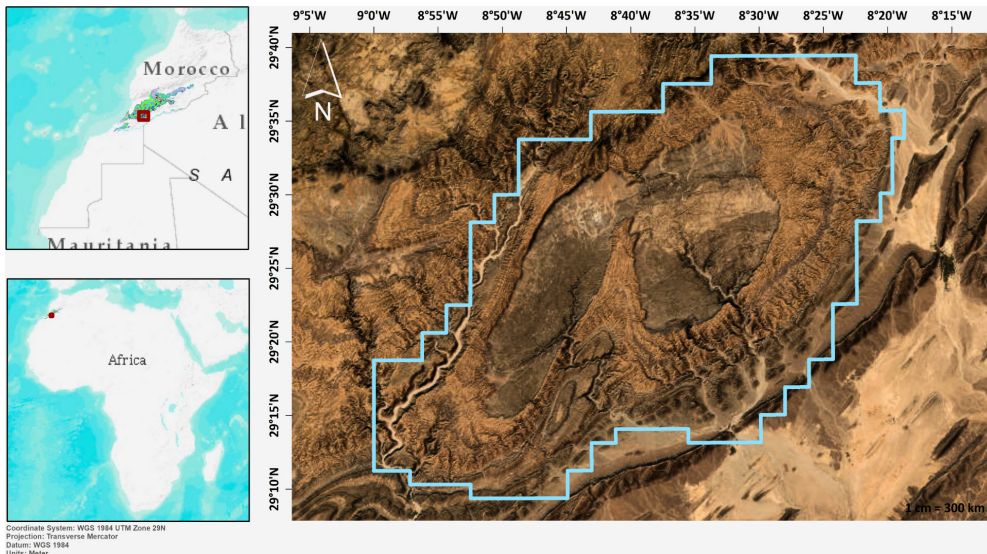


Fig. 2. Geographical setting of Tagragra d’Akka inlier

Geological Setting

Anchored in the Precambrian geological context [48–50], the Tagragra d’Akka inlier is distinguished by its Paleoproterozoic basement and its unconformably overlain Infra-Cambrian calcareous-dolomitic cover [52–54].

The basement (characterized by lithological complexity) reveals a predominantly metamorphic composition that is dominated by metashale and schists [52, 55]. This basement is divided into two distinct lobe-like structures – one eastern, and one western [56, 57].

The eastern lobe is marked by the presence of a two-mica leucogranite and biotite granite intrusions that date from the Eburnean orogeny [56, 57]. These intrusive masses are found within lower Proterozoic metamorphic and volcano-sedimentary

formations. Dykes of gabbro, granodiorite, and dolerite cut across these formations, thus emphasizing the lithological diversity of this region [48, 52, 56–60].

The western lobe is primarily composed of metamorphic and volcano-sedimentary rocks from the Paleoproterozoic Era; it is also intersected by dolerite and rhyodacite dykes [53, 61].

The calcareous-dolomitic cover from the Adoudounian age dates back approximately 540 million years [52–54]; it consists of dolomitic, limestone, and shale formations, which add a temporal dimension to the rich geological history of the inlier. This cover contributes to the complex lithological configuration of the region [62].

The influence of two major orogenic phases (the Eburnean cycle [marking the early Paleoproterozoic structures], and the Pan-African cycle [occurring at the end of the Proterozoic]), has shaped the entire inlier. These tectonic events led to the formation of the metamorphic basement and the sedimentation of the calcareous-dolomitic cover. The structural complexity of the region is evident through the presence of schistosity, folds, fault fractures, veins, joints, and breccias [48, 49, 50, 52, 55].

Distributed into three distinct families (S1, S2, and S3), the schistosity within the Tagragra d' Akka inlier play a crucial role in the structural characterization of the region. The S1 family (parallel to the stratification and associated with the Eburnean cycle) reflects the early Paleoproterozoic structures, while the S2 and S3 families are closely related to the Pan-African cycle (highlighting the more recent geological evolution of the inlier). Folds have resulted from compressive stresses (primarily oriented NE-SW), while fractures (induced by tensile forces) align along an NNW-SSE orientation [52, 54, 55, 59, 60, 63, 64].

Furthermore, the inlier hosts notable gold deposits, such as the Irbiben deposit, where mineralized formations (especially quartz veins) emerged during the Pan-African cycle [52–54].

This geological and geographical description of the Tagragra d' Akka inlier establishes a solid foundation for the application of modern lithological-mapping methods. A deep understanding of the local geology and lithological features that were outlined above will be essential for interpreting the results and optimizing the accuracy of the proposed lithological-mapping technique.

The geological map in Figure 3 was digitized from published maps of Marrakech (1:500,000), Tafraout (1:100,000), and Tamazrar and Sidi Bouaddi (both 1:50,000); this shows the geological setting of the Tagragra d' Akka inlier.

2.2. Data Collection

The data that was utilized for this study was derived from satellite images that covered the study area. Multispectral (MS) scenes that were captured by the European Space Agency's (ESA's) Sentinel-2A [65] and panchromatic (PAN) images from ALOS PRISM L1B [66] (Panchromatic Remote-sensing Instrument for Stereo Mapping), which were extracted from the archives (from July 2006 to March 2011) of the Japan Aerospace Exploration Agency (JAXA), were employed.

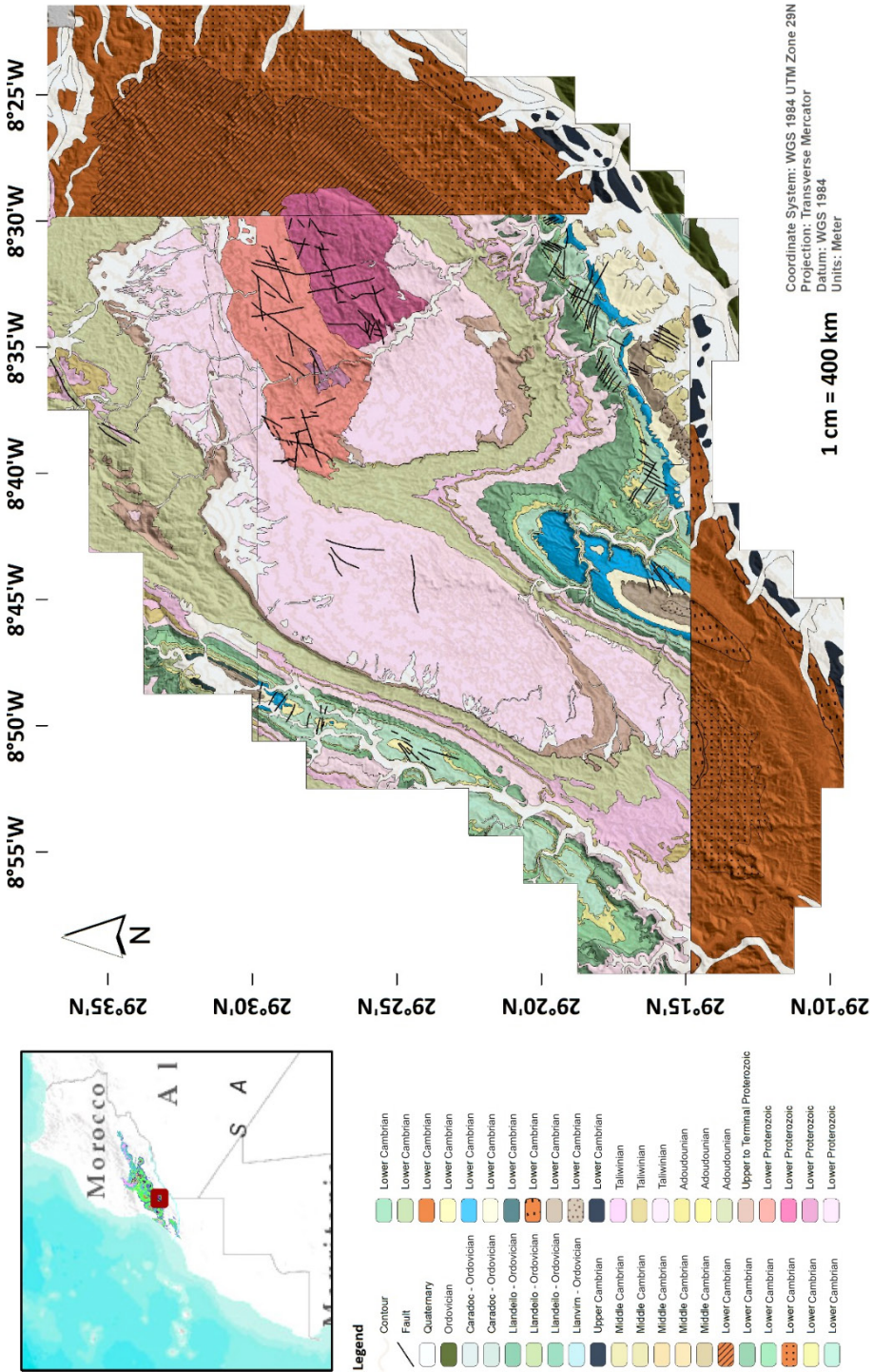


Fig. 3. Geological map of Tagragra d' Akka inlier based on Marrakech (1:500,000), Tafraout (1:100,000), and Tamazrar and Sidi Bouaddi (both 1:50,000) maps

The Sentinel-2A images were acquired on July 20, 2023, with a cloud coverage of 0%; this ensured the clear observation of the ground surface. The Sentinel-2A data was processed at Level-2A, meaning that it had undergone orthorectification and atmospheric corrections, which improved the reliability of the surface-reflectance data for lithological analysis.

The ALOS PRISM L1B images were obtained from a mosaic of six cloud-free scenes that were captured between July and October 2008. This high-resolution panchromatic data (at a 2.5-meter resolution and acquired under favorable illumination conditions) provided the spatial detail that was necessary for precise lithological mapping (when combined with the Sentinel-2A multispectral data).

This combination of the MS and PAN images provided the spatial and spectral resolutions that were necessary for conducting a comprehensive analysis of the lithological characteristics of the study area.

Table 1 shows the characteristics of both Sentinel-2A and ALOS PRISM L1B.

Table 1. Spectral characteristics and data-access information for Sentinel-2A and ALOS PRISM L1B satellites

Satellite image	Spectral band	Wavelength [nm]	Spatial resolution [m]	Swath width [km]	Data access	Link to data
Sentinel-2A	Band 1 – Coastal aerosol	443.9	60	290	Open access	https://dataspace.copernicus.eu/explore-data
	Band 2 – Blue	496.6	10			
	Band 3 – Green	560.0	10			
	Band 4 – Red	664.5	10			
	Band 5 – Veg. Red Edge	703.9	20			
	Band 6 – Veg. Red Edge	740.2	20			
	Band 7 – Veg. Red Edge	782.5	20			
	Band 8 – NIR	835.1	10			
	Band 8A – Veg. Red Edge	864.8	20			
	Band 9 – Water Vapor	945.0	60			
	Band 10 – SWIR Cirrus	1373.5	60			
	Band 11 – SWIR	1613.7	20			
Band 12 – SWIR	2202.4	20				
ALOS PRISM	Panchromatic	520–770	2.5	35	On demand	https://earth.esa.int/eogateway/catalog/alos-prism-l1b

2.3. Pansharpening

Improving the resolution remains a crucial step in making the most of the information that is provided by optical satellite images [67]. The image-fusion technique, which involves combining image bands of different resolutions to create a new image with the best characteristics from all of the input data [68–70], can be used as a tool to increase spatial resolution [71].

In our article, the high-resolution (2.5 m) ALOS PRISM L1B PAN image was fused with the low-resolution (20 and 10 m) Sentinel-2A MS images in a process that is known as pansharpening [71, 72].

The algorithm that was used for the pansharpening is known as color normalized spectral sharpening (CNSS) and was chosen for (1) its ability to preserve spectral and geometric information from MS images and (2) its support for multiple input bands [73, 74]:

$$CN_Sharpened = \frac{InputBand \cdot SharpeningBand \cdot Num_Bands_In_Segment}{Input_Bands_In_Segment + Num_Bands_In_Segment} \quad (1)$$

where:

CN_Sharpened – output sharpened image (created by enhancing resolution or details of multispectral band),

InputBand – multispectral band to be sharpened (usually with lower spatial resolution);

SharpeningBand – high-resolution band (often panchromatic) that is used to enhance InputBand,

Num_Bands_In_Segment – total number of bands in segment that are used for sharpening,

Input_Bands_In_Segment – sum of input bands in segment (based on spatial and spectral characteristics of input image).

Although other fusion methods such as Gram–Schmidt, Discrete Wavelet Transform, and A Trouw Wavelet Transform were available, our study relied on the CNSS method due to its efficiency and faster processing times [75]. Given the extensive surface area of our region of interest, pansharpening would demand significant computational resources. The CNSS method provided an optimal balance between processing efficiency and the preservation of spectral fidelity while enhancing spatial detail; this made it the ideal choice for our lithological-mapping objectives.

The spatial resolutions of the Sentinel-2A bands were enhanced to a resolution of 2.5 m through their fusion with the ALOS PRISM L1B PAN band. The resulting pansharpened bands displayed a spatial resolution of 2.5 m (as illustrated in Figure 4); this retained the spectral characteristics of the original MS bands.

From the higher-resolution Sentinel-2A bands, only visible to near-infrared (VNIR) bands B2, B3, and B4 and short-wave infrared (SWIR) bands B11 and B12 were selected for the subsequent stages of the study [76].

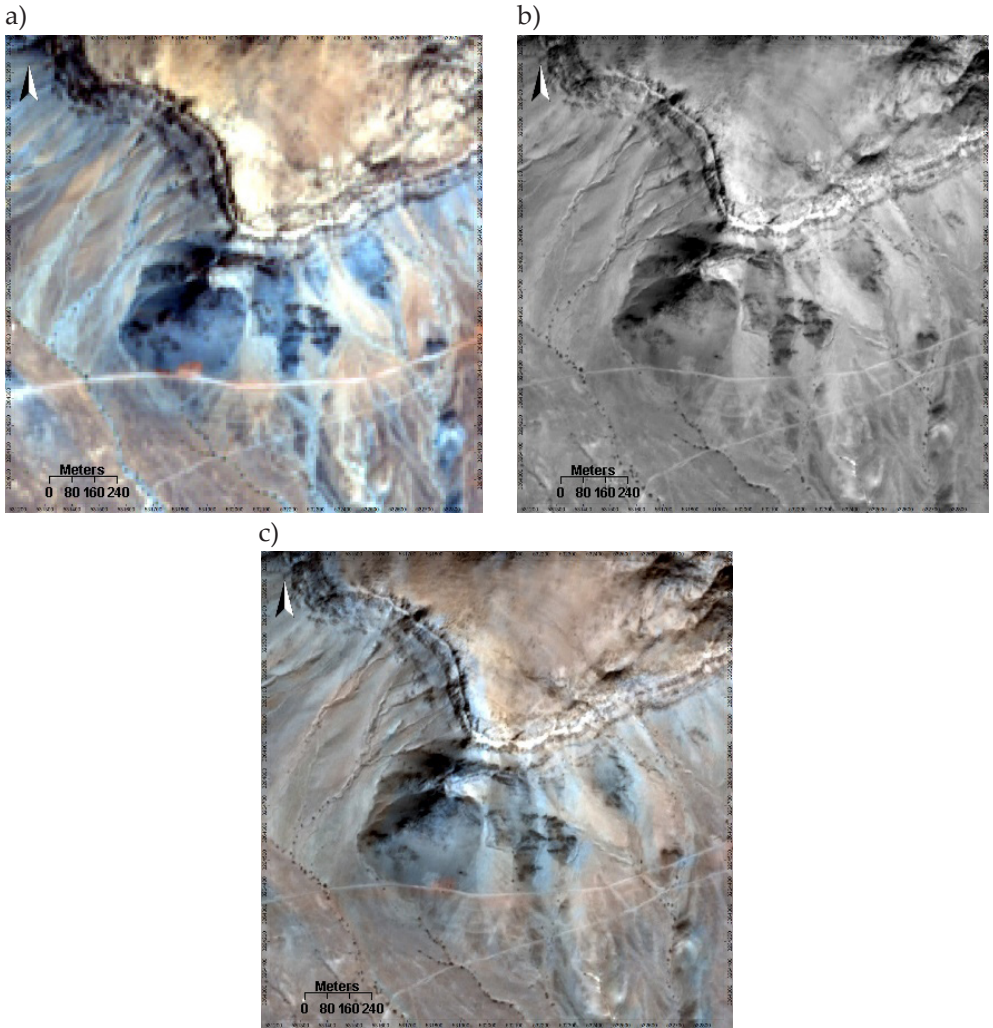


Fig. 4. Resolution enhancement through pansharpening:
a) S2A MS True Color Composite, 10-meter spatial resolution;
b) ALOS PRISM L1B PAN band, 2.5-meter spatial resolution;
c) High-res MS True Color Composite, 2.5-meter spatial resolution

2.4. Principal Component Analysis (PCA)

The high-resolution MS bands were integrated into a principal component analysis (PCA). PCA is a statistical technique that is aimed at reducing the dimensionality of a data set while preserving its variability [77]. In remote sensing, this enhances the relevance of the pixels for geological applications based on their specific spectral signatures [78–80].

To initiate PCA, mathematical calculations were performed earlier on the high-resolution MS bands – particularly, by establishing ratios between specific bands to facilitate the distinctions between lithological formations. These ratios were selected based on the geological context, with the goal of optimizing the differentiation of the mineral and lithological-formation characteristic of the region.

The calculated ratios included the following:

- BandRatio1 (B04/B03: Red/Green),
- BandRatio2 (B11/B02: SWIR/Blue),
- BandRatio3 (B12/B04: SWIR/Red).

BandRatio1 (B04/B03: Red/Green). This ratio was chosen to highlight oxidized formations and minerals that contained iron oxides, such as those that are found in metamorphic rocks (schists) and weathered deposits (which were thought to be abundant in this area). Commonly resulting from metamorphic and alteration processes minerals like hematite and goethite typically exhibit strong absorptions in the red band (B04) and higher reflectance in the green band (B03), thus facilitating their identification in altered zones [76]. This ratio was, therefore, effective for locating altered zones and oxidized mineralizations that were linked to tectonic structures.

BandRatio2 (B11/B02: SWIR/Blue). This ratio targeted the hydrated minerals (particularly, clays) that may have been present in the schist and metashale formations of the Paleoproterozoic basement as well as in the altered dolomitic formations in the cover layer. Formed from the alteration of schists and other metamorphic rocks, clays exhibit characteristic absorption in the SWIR (B11) due to their OH bonds, while reflectance in the blue band (B02) enhances this contrast [76]. This ratio is essential for detecting clay-bearing zones, which are often associated with metamorphism and hydrothermal alteration in tectonically active regions such as Tagragra d’Akka.

BandRatio3 (B12/B04: SWIR/Red). This ratio was used to detect siliceous minerals like quartz, mica, and feldspar, which are abundant in the granite intrusions (biotite granite and two-mica leucogranite) and the quartz veins that are associated with the region’s gold deposits. Siliceous minerals and granite intrusions are characterized by increased reflectance in the SWIR (B12) and absorption in the red band (B04), making this ratio effective for distinguishing silicate-rich units [76]. In the Tagragra d’Akka area, this ratio was particularly relevant for distinguishing quartz veins from other metamorphic and volcano-sedimentary formations.

The resulting images from the calculated band ratios are shown in Figure 5.

The calculated ratios were then used in PCA within SAGA GIS [81] – open-source software that is commonly used in geoscientific applications. In SAGA GIS, the band-ratio images are input into the PCA algorithm, and a set of uncorrelated principal components (PCs) that capture the maximum spectral variability within the data are generated.

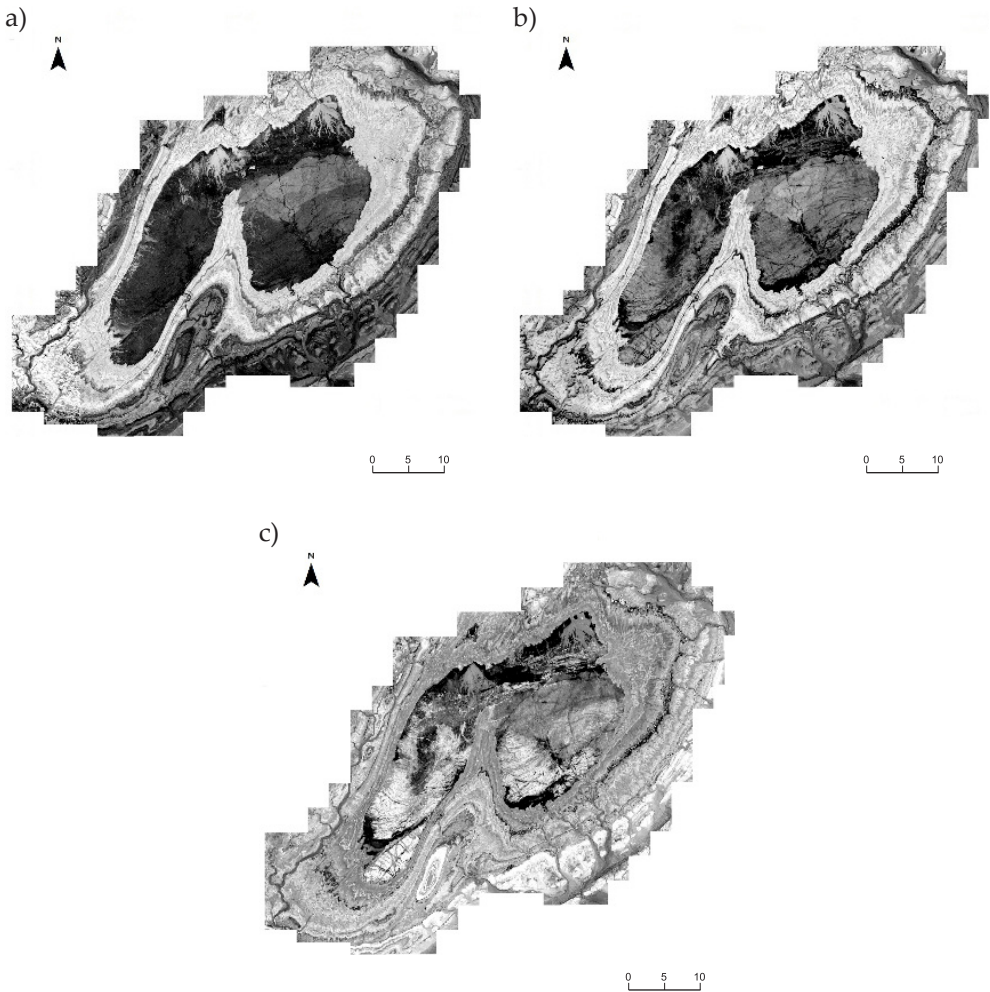


Fig. 5. Calculated band ratios:

a) $\text{BandRatio1} = B04/B03$; b) $\text{BandRatio2} = B11/B02$; c) $\text{BandRatio3} = B12/B04$

From the resulting PCs, three were selected to represent most of the spectral variability of the lithologies: PC1, PC2, and PC3. These exhibited most of this variability; as such, they were combined into a color composite for the red, green, and blue channels, respectively.

This approach allowed for visualizations of the different lithologies in the region in a distinct and contrasting manner within single composite images (Fig. 6).

Resulting composite image from PCA showed a very clear distinction between the carbonate and detrital formations. The metamorphic and igneous formations displayed a slightly less pronounced but still identifiable contrast.

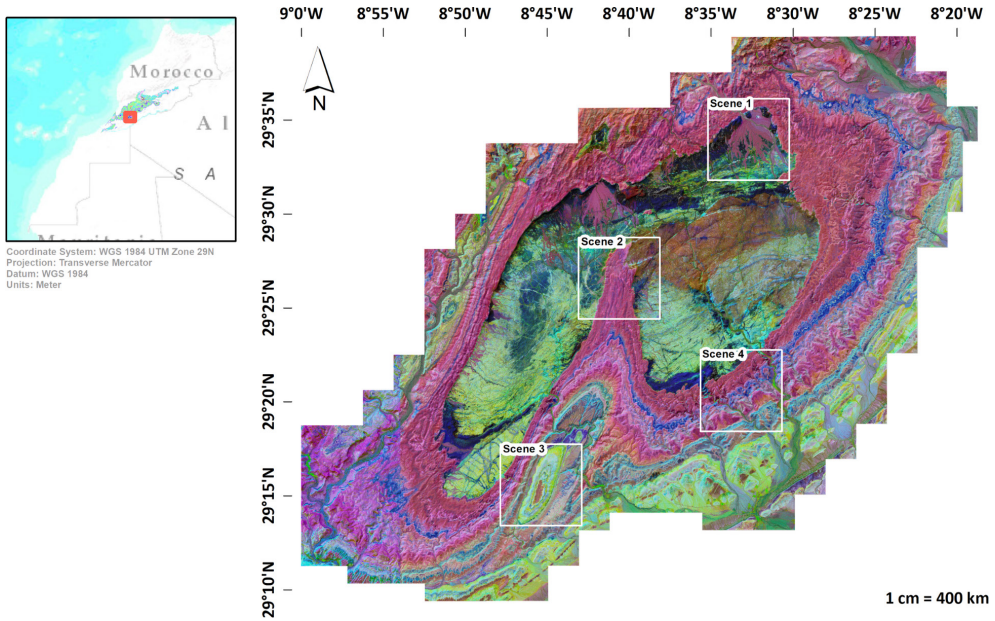


Fig. 6. Composite image of Tagragra d' Akka inlier

2.5. Unsupervised Segmentation

The resulting image from PCA was provided to a segmentation algorithm that was aimed at grouping those pixels with similar characteristics into clusters [82, 83]. The segmentation fell within the domain of computer vision and image-processing applications – both disciplines of artificial intelligence [84]. While there are several segmentation algorithms, the one that was used here was Mean Shift – a clustering method that was proposed by Fukunaga and Hostetler [85]; it was developed in 1975 but only became widely known in 1995 [86]. This method was chosen for its advantages [87], including (1) its non-parametric and iterative nature, (2) its lack of a requirement for a pre-defined number of clusters, and (3) its independence from the shapes of the clusters [88]:

$$M_h(x) = \frac{1}{k} \sum_{x_i \in S_k} (x_i - x) \tag{2}$$

where:

- $M_h(x)$ – function that represents measure or value that is calculated at point x ,
- k – normalizing constant or total number of points x_i in subset S_k
- $\sum_{x_i \in S_k}$ – summation over all points x_i that belong to subset S_k
- x_i – individual points within subset S_k
- x – specific point at which $Mh(x)$ is evaluated,
- $(x_i - x)$ – difference between each point x_i in S_k and point x .

The main objective of this segmentation was to automatically extract any out-cropping formations. The result of this step was an image that was classified into clusters, with each cluster corresponding to a distinct lithology (Fig. 7).

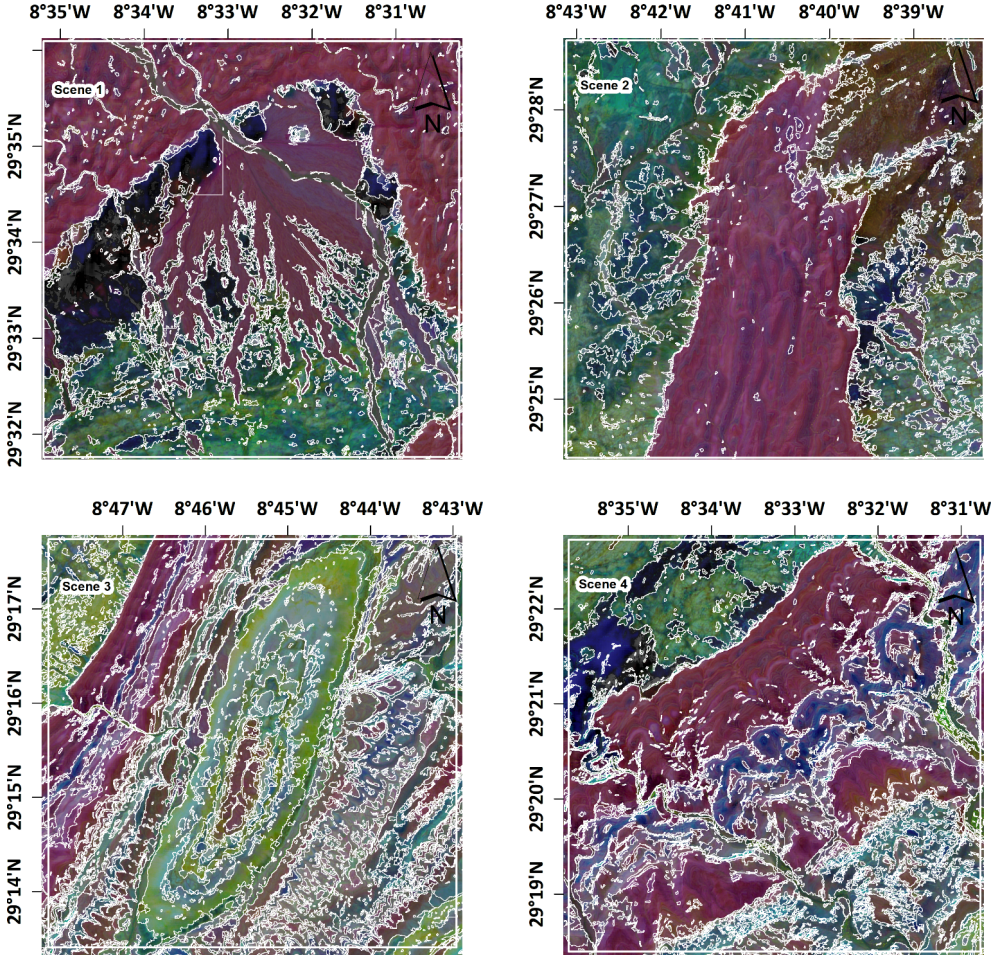


Fig. 7. Vector clusters of similar pixels, with close-up images highlighted in Figure 6

The applied segmentation demonstrated the ability to discern subtle details in geological structures, as is evident in Scenes 1, 2, 3, and (especially) 4 (Fig. 7). The contours that were delineated by this segmentation were remarkably fine and precise, thus providing a cartographic representation of exceptional quality and ensuring a detailed characterization of the different geological formations in the study area (Fig. 8).

These results highlight the capability of high resolution in capturing the nuances of a landscape, thus paving the way for the generation of large-scale maps that offer comprehensive representations of geological features.

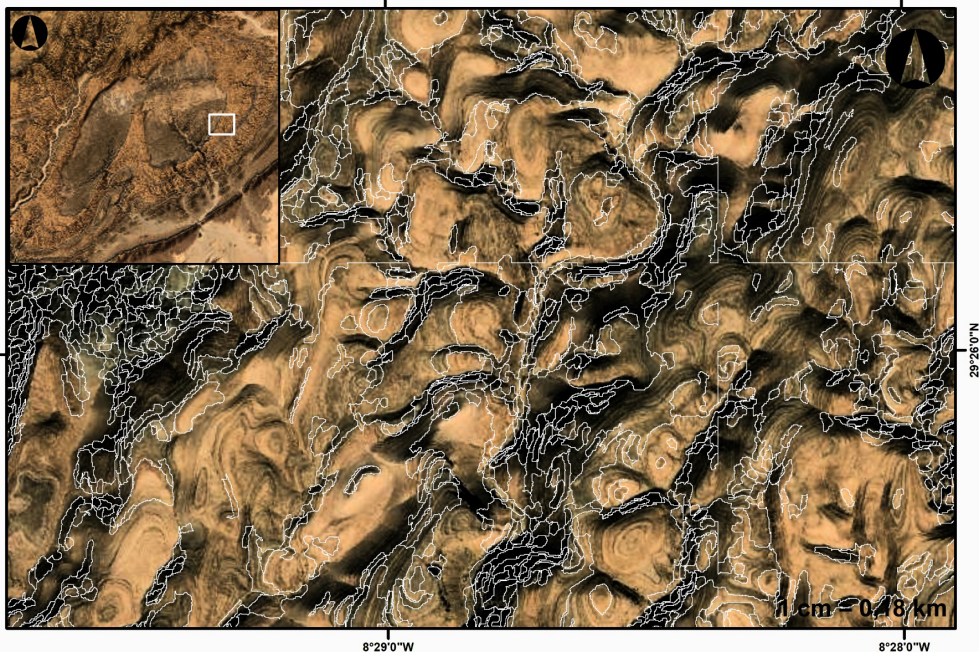


Fig. 8. Overview of segmentation details in true-color composite

Subsequently, the zonal statistics were calculated from the pixel values of the raster that resulted from PCA within the boundaries of the segmented units to perform meaningful analyses and interpretations [89]. Figure 9 explains the process of this step.

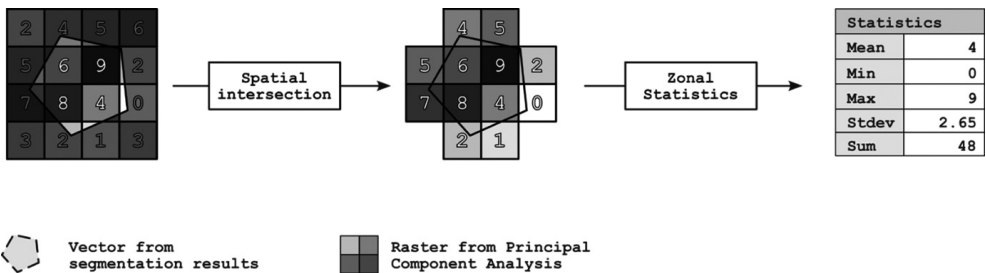


Fig. 9. Zonal-statistics process

2.6. Supervised Classification

In the field of image analysis, supervised classification is the process where pixels are assigned to predefined classes [90]. In geology, supervised classification involves the grouping of similar pixels into classes that correspond to different rock types by comparing the pixels with each other and with those whose lithologies are known [91].

For a lithological study, remote sensing enables the exploitation of any differences in the physical and chemical properties of rocks. The variations among the rocks result in reflections of electromagnetic energy at different wavelengths, thereby allowing for the identification of those spectral characteristics that are related to the mineralogy of the rocks. Those methods that are based on the spectrum are commonly used for automated lithological mapping or classification [92].

As assemblies of minerals, rocks exhibit higher compositional complexities than individual minerals do. While defining diagnostic spectral curves for rocks is a challenge, it is possible to comprehensively describe their spectral characteristics based on those of constituent minerals. Among the two methods that use spectral signatures (namely, solar reflection and thermal-IR reflection), our approach focused on a solar reflection (VNIR + SWIR) analysis. This method relies on models to understand the influences of minerals and textures on the spectra [76].

To establish the specific spectral signatures for each rock type, we utilized the Sentinel Application Platform (SNAP) software [93]. SNAP allows for the extractions of reflectance spectra across the VNIR-SWIR bands, thus facilitating the identification of mineralogical compositions by analyzing the spectral responses at targeted wavelengths. In this study, we selected representative pixels for each lithological type in the Tagragra d'Akka inlier and generated spectral signatures; these were then compared with the reference spectra for the minerals that were typical of each rock type (such as iron oxides, clays, and carbonates) [76]. This comparative approach confirmed the lithological identities of the various classes.

2.7. Data Preparation

Based on previous geological works in the region [49, 53, 56], the main lithological formations that can be identified include volcanic, metamorphic, carbonate, and detrital rocks. Before starting the sampling process, the specific spectral signatures for each rock type were defined in order to characterize the samples and train the model (Table 2).

To ensure an adequate discrimination among the rock types despite their generally similar spectral behaviors at Sentinel-2's spectral resolution, we employed class-separability measures such as the Jeffries-Matusita distance and divergence indices [94].

Figure 10 clearly illustrates these spectral signatures, presenting reflectance values as functions of the wavelengths for all of the lithologies.

Table 2. Reflectance values of each rock type at Tagragra d' Akka inlier in relation to wavelengths

Rock type	Band λ [nm]											
	B1 (443)	B2 (490)	B3 (560)	B4 (665)	B5 (705)	B6 (740)	B7 (782)	B8 (842)	B8A (865)	B9 (945)	B11 (1610)	B12 (2190)
DoL	0.169	0.164	0.200	0.314	0.336	0.357	0.376	0.374	0.383	0.229	0.498	0.426
LiM	0.171	0.166	0.198	0.301	0.324	0.339	0.351	0.338	0.354	0.196	0.460	0.390
LeG	0.175	0.175	0.213	0.297	0.302	0.322	0.331	0.335	0.342	0.193	0.418	0.336
PG	0.168	0.169	0.198	0.273	0.275	0.292	0.311	0.307	0.315	0.163	0.348	0.290
GD	0.168	0.171	0.200	0.275	0.291	0.298	0.313	0.302	0.314	0.173	0.386	0.323
DoL	0.156	0.146	0.171	0.258	0.277	0.289	0.303	0.301	0.310	0.194	0.363	0.306
TA	0.156	0.147	0.168	0.240	0.258	0.271	0.282	0.271	0.281	0.150	0.236	0.206
CoG	0.154	0.162	0.180	0.243	0.240	0.257	0.258	0.269	0.257	0.130	0.234	0.180
SiS	0.156	0.140	0.154	0.215	0.240	0.264	0.281	0.268	0.287	0.159	0.282	0.243
MeS	0.157	0.155	0.180	0.235	0.235	0.242	0.255	0.246	0.253	0.131	0.340	0.304
QuS	0.155	0.143	0.161	0.215	0.227	0.234	0.247	0.238	0.246	0.134	0.322	0.298
SiIS	0.161	0.146	0.153	0.207	0.223	0.238	0.249	0.236	0.252	0.147	0.234	0.214
SaS	0.157	0.149	0.169	0.214	0.223	0.232	0.242	0.234	0.234	0.121	0.327	0.282
Quz	0.153	0.139	0.149	0.196	0.210	0.214	0.227	0.216	0.226	0.123	0.313	0.282
ScT	0.144	0.134	0.150	0.187	0.190	0.199	0.204	0.198	0.203	0.104	0.218	0.187
Tuf	0.151	0.138	0.141	0.179	0.187	0.195	0.199	0.193	0.198	0.118	0.165	0.137
IgB	0.152	0.146	0.153	0.181	0.186	0.195	0.198	0.191	0.196	0.109	0.207	0.181
SiS	0.149	0.129	0.131	0.147	0.167	0.166	0.176	0.158	0.173	0.097	0.225	0.186

DoL – Dolomitic limestone; LiM – Limestone; LeG – Leucogranite; PG – Porphyritic granite; GD – Granite granodiorite; DoL – Dolomite; TA – Trachyandesite; CoG – Conglomerate; SiS – Silty sandstone; MeS – Metashale; QuS – Quartzitic sandstone; SiIS – Siltstones; SaS – Sandy shale; Quz – Quartzite; ScT – Schiste; Tuf – Tuff; IgB – Ignimbrite; SiS – Silty shale.

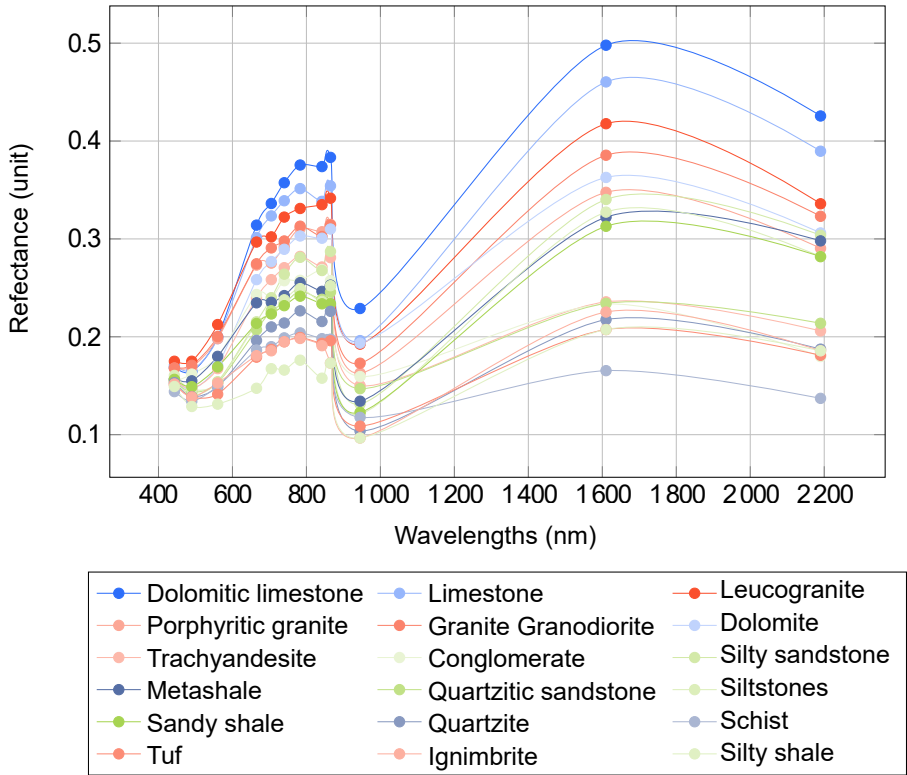


Fig. 10. Spectral profiles of different reflectance responses of rock types

Once the spectral signatures were determined, a set of samples was generated to initiate the sampling process from the image; these carefully positioned samples represented different combinations of spectral features. This data was then used to train our model, thus facilitating a comprehensive analysis of the various rock types based on the previously defined spectral information.

2.8. Data Splitting

The preprocessed data was split into two sets in order to ensure robust model training and evaluation. Specifically, the data was divided on a per-class basis (with 70% allocated for training and 30% for testing), thus maintaining a proportional representation of each lithological unit in both sets. This approach supported balanced-model training and reliable assessment by preserving the inherent class distribution [95]. Each lithological unit's samples were randomly selected for the training and testing based on this split, thus reducing any sampling bias and enhancing the model's ability to generalize across the study area. The spatial distribution of these samples is illustrated in Figure 11, while Table 3 outlines the exact pixel counts per lithological unit in each set.

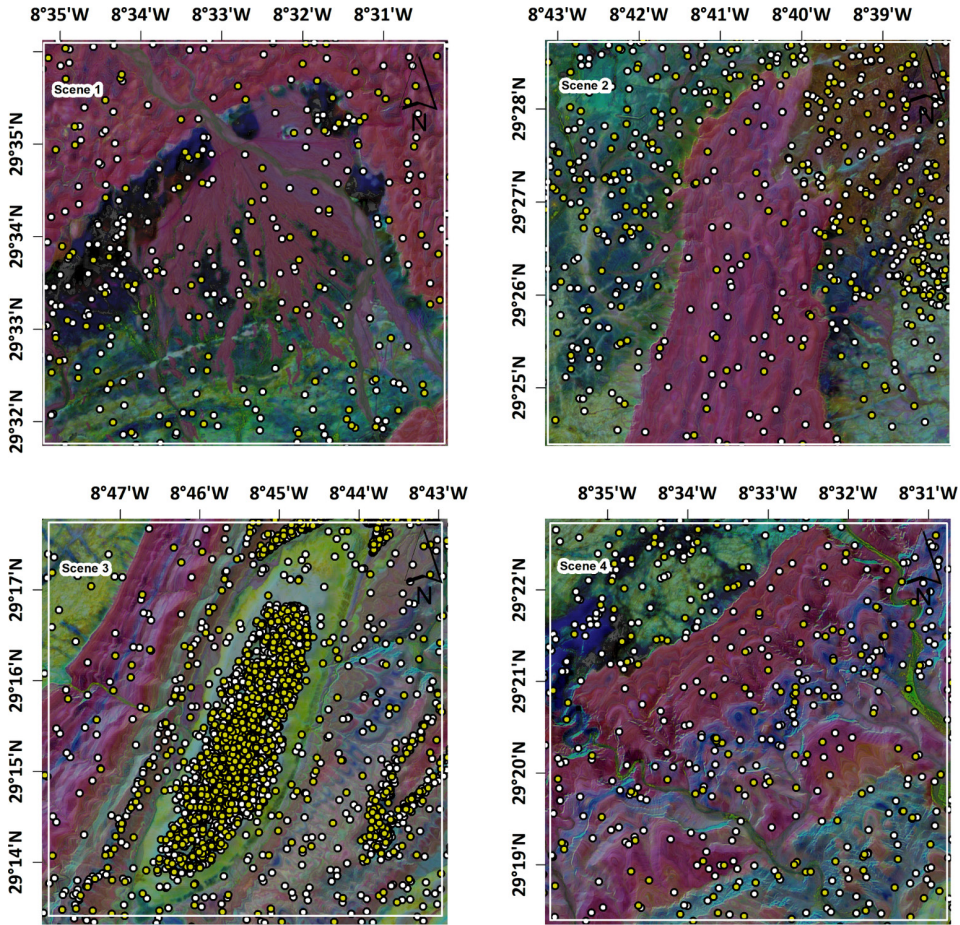


Fig. 11. Samples from different locations in Tagragra d' Akka inlier

In supervised classification tasks such as lithological mapping, class imbalance is a well-known challenge – particularly with classifiers like SVM, which can be sensitive to overrepresented classes. Table 3 highlights the uneven distribution of the training samples among the lithological units, which arose due to the natural variability in the occurrence of each rock type across the study area.

To mitigate the issue of class imbalance, additional strategies can be employed. One effective approach is using a class-weight parameter, which adjusts the importance of each class during model training, thus ensuring that underrepresented classes receive adequate attention. Another common method involves oversampling techniques such as the Synthetic Minority Over-sampling Technique (SMOTE), which generates new samples for minority classes by interpolating between the existing ones. These methods help create a more balanced representation of the classes in a training set, potentially improving the classification accuracy for less-prevalent lithological units.

Table 3. Number of pixel samples taken for each rock type in Tagragra d'Akka inlier

Lithological unit	Training samples [pixels]	Testing samples [pixels]
Dolomitic limestone	965	498
Limestone	490	293
Leucogranite	879	356
Porphyritic granite	321	137
Granite granodiorite	2015	1002
Dolomite	7878	2459
Trachyandesite	271	147
Conglomerate	1819	847
Silty sandstone	856	356
Green schist (metashale)	3442	1865
Quartzitic sandstone	303	118
Siltstones	1920	802
Sandy shale	140	85
Quartzite	122	51
Spotted schist	428	207
Tuff	133	74
Ignimbrite	605	398
Silty shale	179	61

2.9. Model Training

The training process is crucial in developing a lithological classification model; it involves providing a training data set for a machine-learning algorithm, thus allowing it to construct an adequate representation of the spectral features of the targeted lithological formations.

In this study, the chosen machine-learning algorithm for classification was SVM; such an algorithm stands out for its ability to define a hyperplane in a multidimensional space, effectively separating the data into different classes while maximizing the margin between these classes [96]. This intrinsic feature makes SVM particularly robust, reducing the risk of overfitting as compared to other classifiers and enhancing its ability to generalize models to unknown data sets.

The SVM algorithm was deliberately selected due to its specific advantages in the context of lithological classification. The intrinsic complexity of rock spectra (often characterized by nonlinear patterns) benefits from the efficiency of SVM in handling such complex spectral structures.

To develop our model, we used Orfeo ToolBox’s [97] machine-learning functionalities, which provided a streamlined approach for setting up and training the classifier without the need for exhaustive parameter-tuning. We defined a linear SVM kernel, and we used C-support vector classification (CSVC) as the model type within the TrainVectorClassifier tool.

After executing the classifier, we applied the generated model to the vector data in order to classify the image based on the spectral signature patterns that were identified during the training.

2.10. Model Evaluation

Evaluating a machine-learning model involves using it on new data, thereby making predictions on unknown data sets.

In this study, the pretrained lithology-detection model was utilized to classify the rest of the Tagragra d’Akka region. To assess the performance of the developed lithology-detection model, a confusion matrix was calculated. The confusion matrix expressed the classification results by dividing them into four categories: true positive, false positive, false negative, and true negative (Table 4). Using these four categories, the model could be evaluated in various ways [98].

Table 4. Confusion-matrix parameters

Classifier output		Actual class	
		0	1
Predicted class	0	True negatives (TN)	False negatives (FN)
	1	False positives (FP)	True positives (TP)

In the context of a confusion matrix, true positives are correctly classified as positive pixels, and false positives are negative pixels that are labeled as positive by the model (and vice versa for the true and false negatives):

$$CM = \begin{bmatrix} m_{11} & \cdots & m_{1c} \\ \vdots & \ddots & \vdots \\ m_{c1} & \cdots & m_{cc} \end{bmatrix} \tag{3}$$

where:

- CM – confusion matrix, which is used to evaluate performance of classification model by comparing predicted and actual classes,
- c – total number of classes in classification problem.

Several performance metrics were used based on the confusion matrix to evaluate the classification performance. For those data sets with class imbalances (and in the case of multiclass classification), the recommended performance evaluation metrics included precision, recall, the F1 score, the overall accuracy, and the Cohen kappa score [99]. Precision is the proportion of the data that a model correctly identifies as true; while recall is the true positive rate; i.e., the proportion of the positive examples that are correctly identified. The F1 score is the harmonic mean of precision and recall, while the overall accuracy is the proportion of correctly labeled examples. Cohen’s kappa coefficient is a metric that compares any observed accuracy to the expected accuracy; it assesses how well the model can separate instances into the correct classes. According to Landis and Koch [100], a kappa score of 0.00–0.20 corresponds to a slight agreement, 0.21–0.40 to a fair agreement, 0.41–0.60 to a moderate agreement, 0.61–0.80 to a substantial agreement, and 0.81–1.00 indicates a nearly perfect agreement by the classifier. Table 5 summarizes the equations of the used evaluation metrics.

Table 5. Evaluation metric equations

Metrics	Equation
Precision (user’s accuracy [UA])	$Precision = \frac{TP}{TP + FP}$
Recall (producer’s accuracy [PA])	$Recall = \frac{TP}{TP + FN}$
F1 score	$F_1 \text{ Score} = 2 \cdot \frac{Precision \cdot Recall}{Precision + Recall}$
Overall accuracy	$Accuracy = \frac{TP + TN}{TP + TN + FP + FN}$
Kappa coefficient	<p data-bbox="497 1410 560 1434">where:</p> $K_c = \frac{P_o - P_e}{1 - P_e}$ $P_o = \frac{TP + TN}{TP + TN + FP + FN}$ $P_e = \frac{(TP + FN)(TP + FP) + (FP + TN)(FN + TN)}{2 \cdot (TP + TN + FP + FN)}$

3. Results

3.1. Lithology-Detection-Model Evaluation

During the testing of the lithology-detection model on the new samples from the Tagragra d’Akka inlier, the evaluation showed that the model successfully identified 16 out of the 18 rock classes on which it had been trained. Due to their comparable spectral properties, three classes (tuff, ignimbrite, and trachyandesite) were combined into a single class (which we designated “volcanic-detritic complex”).

The model evaluation involved a thorough examination of the key metrics, including precision, recall, and the F1 score for each lithological class. These measures provided a detailed understanding of the model’s ability to perform accurate classifications. The results are detailed in Table 6 and in Figure 12.

Table 6. Performance metrics for each rock class

Rock class	Precision [%]	Recall [%]	F1 score [%]
Sandy shale	64	71	67
Siltstones	70	71	70
Limestone	97	79	87
Dolomitic limestone	84	95	89
Volcanic-detritic complex (tuff, ignimbrite, and trachyandesite)	78	74	76
Conglomerate	10	8	9
Silty shale	70	75	72
Dolomite	96	90	92
Silty sandstone	86	89	84
Porphyritic granite	87	87	87
Quartzitic sandstone	88	78	83
Leucogranite	97	85	91
Quartzite	84	77	80
Spotted schist	78	72	75
Green schist (metashale)	86	86	86
Granite granodiorite	84	87	86

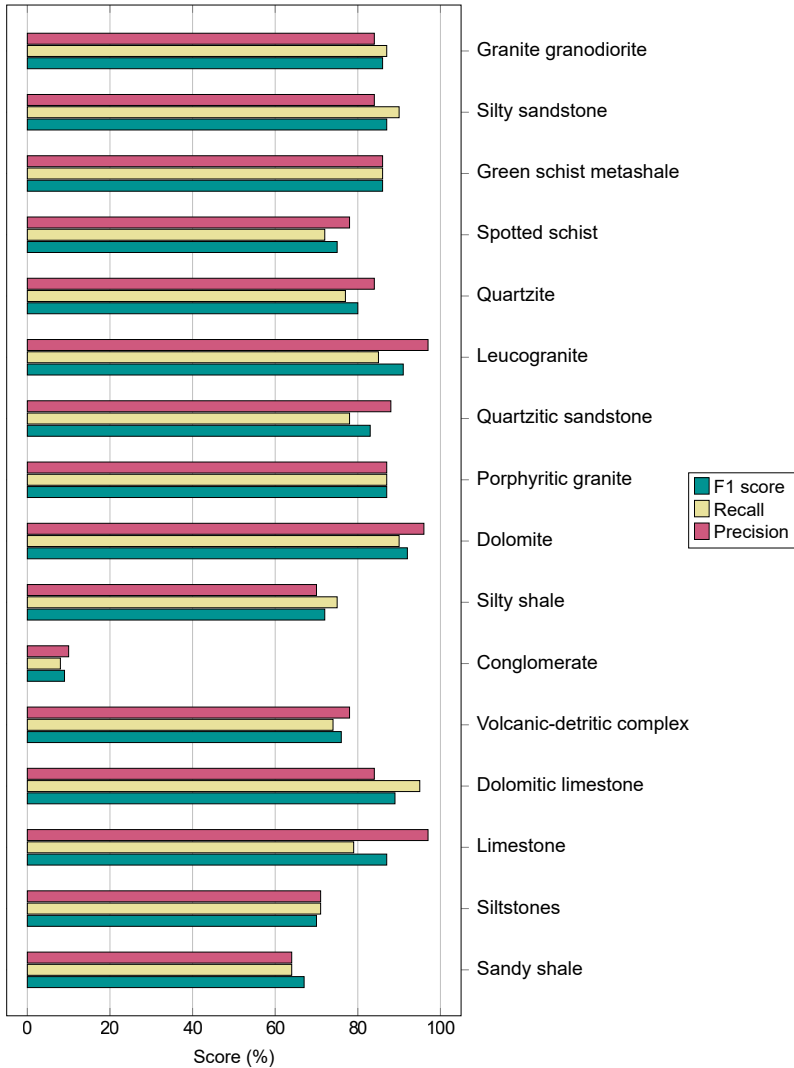


Fig. 12. Model’s performance metrics for different lithological units – precision, recall, and F1 score

The variability in the model performance became apparent, thus revealing its remarkable ability to discern certain lithological classes. Satisfactory precision was demonstrated in the classifications of the sedimentary rocks – especially of the carbonates (ranging between 84 and 97%) and the detrital rocks (between 64 and 84%). On the other hand, the conglomerates displayed the lowest value (10%).

However, the classifications of the metamorphic and igneous rocks showed oscillating precision levels for the metamorphic rocks (between 78 and 86%) and the volcanic rocks (between 78 and 97%). Overall, the results showed that the developed

model demonstrated its general ability to automatically distinguish between the different lithological classes, with marked priorities for the carbonates, followed by the volcanic rocks, then the metamorphic rocks, and, finally, the detrital rocks (presenting average values of 90, 87, 82, and 74%, respectively).

The low precision that could be observed for the conglomerate class highlighted a specific challenge for the developed model in characterizing this lithology; this was mainly due to the heterogeneity of the elements that made up the rock. This paves the way for further investigations in future work.

The evaluation metrics are represented as bar charts for each of the detected lithological classes in Figure 12.

As shown in Table 6, the model’s performance was evaluated for each rock class. Given the data set’s imbalance (with the majority classes potentially affecting the overall accuracy), we included the recall and precision for each class to provide a more comprehensive assessment. This detailed breakdown allows for a clearer view of the model’s effectiveness across all of the rock types, thus ensuring that the minority classes were adequately represented in the evaluation. After measuring the proportions of the correct classifications, the overall accuracy reached 86%; this indicated high model performance. Additionally, the kappa coefficient (which assesses agreement beyond chance) was 84%, suggesting the substantial alignment between the model’s predictions and its actual observations (Table 7).

Table 7. Model-performance metrics

Metric	Value [%]
Overall accuracy	86
Kappa coefficient	84

3.2. Lithological Classification Map

The lithological classification map (Fig. 13) represents the culmination of our lithological-mapping approach.

Leveraging the good performance of the machine-learning model, this map provides a precise and detailed depiction of the various lithological classes in the Tagragra d’Akka inlier. Additionally, it highlights cryptic classes that were not present in the existing geological maps but are similar to 1 of the 16 classes on which the model was trained in their lithological characteristics (as shown by the black box on the map). These newly identified classes were labeled “Unmapped” (e.g., sandy shale – Unmapped 1; spotted shale – Unmapped 2); this label reflected that these classes ages were not determined. Further dating studies are needed to provide a comprehensive identification of these formations.

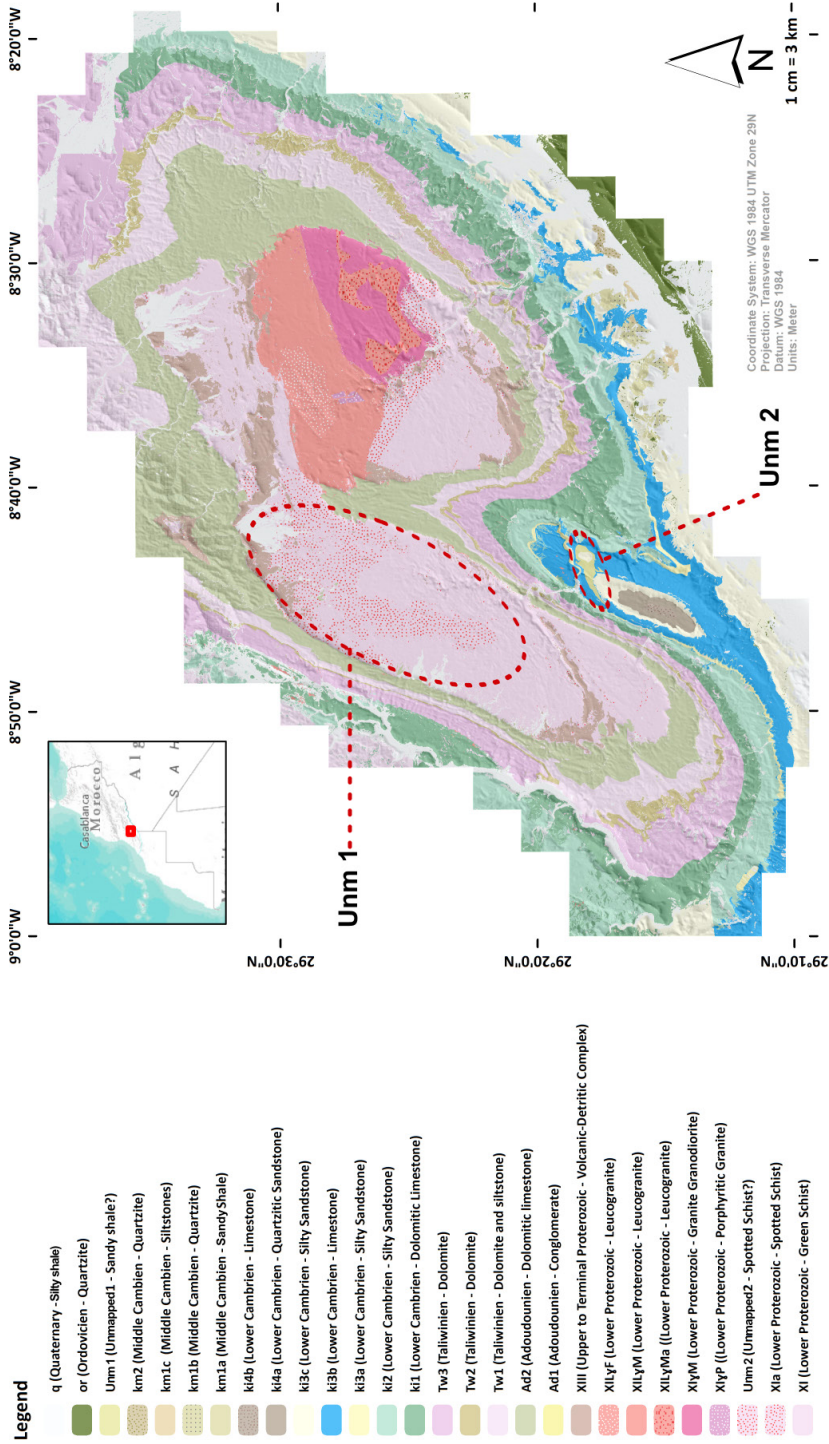


Fig. 13. Lithology map that was produced by lithology-detection model ('Unm' - unmapped)

4. Discussion

4.1. Comparison with Other Methods

Following a comprehensive evaluation of our lithological-mapping method, we came to the conclusion that we developed an effective methodology in terms of spatial resolution and processing speed, thus placing it among similar approaches that have been introduced in other studies [5, 19, 92, 101–106]. The diversity of these methods enables a transition from traditional approaches (which are often costly, time-consuming, and prone to human error) to a faster, more accurate, and cost-effective digital workflow. Our study offers the following advantages:

Spatial Resolution

A crucial difference between the approach that was adopted in this article and existing methods lies in the spatial resolution that can be achieved. Unlike most studies that use Landsat images at 30 m [23, 27] or ASTER images at 15 meters [27, 29], our method leverages a panchromatic image from ALOS PRISM L1B and applies it to Sentinel-2A MS bands, thus providing a remarkable resolution of 2.5 m. This advance in spatial resolution contributes to enabling a detailed characterization of lithological formations in arid regions. Additionally, the finer spatial resolution facilitates the identification of smaller lithological features, which are often missed at coarser resolutions. This enhancement is particularly important for regions with complex geologies, where fine-scale variations can be critical for understanding their geological histories and structures.

Our study contributes to the growing amount of research that has focused on enhancing the spatial resolution of satellite imagery. For instance, several studies have utilized WorldView imagery to discriminate lithologies – taking advantage of its high spatial resolution (which reaches 0.3 meters). In one such study, Karimzadeh and Tangestani [104] demonstrated the effectiveness of WorldView-3 imagery in lithological discrimination. In another study, Zengeya et al. [101] showcased how WorldView-2 multispectral data could be used to predict and map nitrogen concentrations, further illustrating the versatility of high-resolution satellite data in environmental monitoring.

Detection Scale

Our method demonstrates an ability to extract lithological details that support the creation of large-scale geological maps. The detailed mapping scale can help with microtectonic studies and mining exploration while also improving mineral exploration by more accurately detecting small geochemical and geophysical features.

Detections of Unmapped Cryptic Areas

A notable contribution of the model lies in its ability to detect areas that have been wrongly mapped in existing geological maps. By identifying previously unexplored areas, the method adds significant value to the updating and enrichment of

geological knowledge (and a reconsideration of past geological events in the Tagragra d' Akka inlier). Moreover, the detection of these unmapped cryptic areas could lead to new discoveries of mineral deposits or other natural resources, potentially driving economic development in a region. The ability to reveal cryptic geological features also contributes to a better understanding of regional tectonics and the evolutionary history of an area, thus providing valuable data for academic research and practical applications alike.

Limitations

Our lithological-detection model has some limitations that are related to its restricted geographical applicability. After being optimized for regions that share similarities with the Tagragra d' Akka inlier in terms of climate, vegetation, alteration, and topography, the model could face challenges in radically different environments. Its sensitivity to these conditions underscores the need for adjustments in order to ensure optimal performance in diverse contexts. Additionally, the dependence on training data and the need for ongoing updates highlight the challenges that are associated with generalizing the model to various geographical areas. These limitations emphasize the need for caution when applying the model outside its initial context while providing avenues for future improvements to increase its versatility. Future work could focus on expanding the training data set to include a broader range of geological settings, thus improving the model. Another potential improvement might be the integration of multi-sensor data; this could enhance the model's ability to generalize across different environments by leveraging complementary information from various remote-sensing platforms.

5. Conclusion and Perspectives

This study has demonstrated the effectiveness of geospatial analysis in one of the complex application fields (geology) by integrating remote sensing and machine learning. The use of machine-learning algorithms such as SVM for lithological remote sensing from pansharpened satellite images led to the creation of a model with an overall accuracy of 86%. This model was trained on an extensive data set that utilized the spectral signatures of each rock class, thus ensuring reliable classification. These findings underscore the considerable potential of this approach to enhance the accuracy of geological maps. By leveraging high-resolution data and machine-learning techniques, this method offers a significant improvement over traditional mapping techniques, providing more-precise and -detailed geological information. The results of this study pave the way for further scientific research, encouraging the re-evaluations and validations of existing geological maps. Moreover, they guide future map production toward methods like this, which can lead to better resource management, exploration, and environmental planning.

Funding

This research received no specific grant from any funding agency in the public, commercial, or not-for-profit sectors.

CRedit Author Contribution

Y. H.: conceptualization, methodology, software, validation, formal analysis, investigation, resources, data curation, writing – original draft preparation, writing.

Y. A.: methodology, software, formal analysis, validation, review, writing.

A. S.: methodology, data curation, validation, review, supervision.

Declaration of Competing Interests

The authors declare that they have no known competing financial interests or personal relationships that could have appeared to influence the work that is reported in this paper.

Data Availability

Public Data: Sentinel 2A Collection https://doi.org/10.5270/S2_-6eb6imz, and ALOS PRISM L1B <https://doi.org/10.5270/AL1-5e400fd>.

Use of Generative AI and AI-Assisted Technologies

No generative AI or AI-assisted technologies were employed in the preparation of this manuscript.

Acknowledgements

We would like to express our sincere gratitude to the European Space Agency (ESA) and the Japan Aerospace Exploration Agency (JAXA) for their invaluable contributions to this research by providing open data from their Sentinel and ALOS programs. The availability of such high-quality satellite data significantly enhanced the scope and accuracy of our study. This research would not have been possible without the commitment of ESA to open science and the free sharing of data (which greatly benefits the scientific community).

References

- [1] Farina P., Catani F., Colombo D., Fumagalli A., Kukavcic M., Marks F., Moretti S.: *Remote sensing: A tool for landslide investigations at a basin scale*. Geophysical Research Abstracts, vol. 7, 2005, pp. 10157–10168.
- [2] Al-Rawashdeh S., Saleh B., Hamzah M.: *The use of remote sensing technology in geological investigation and mineral detection in El Azraq-Jordan*. Cybergeog: European Journal of Geography – Cybergeog: Revue Européenne de Géographie, no. 358, 2006. <https://doi.org/10.4000/cybergeog.2856>.

- [3] Zhang X., Li P.: *Lithological mapping from hyperspectral data by improved use of spectral angle mapper*. International Journal of Applied Earth Observation and Geoinformation, vol. 31, 2014, pp. 95–109. <https://doi.org/10.1016/j.jag.2014.03.007>.
- [4] Masoumi F., Eslamkish T., Abkar A.A., Honarmand M., Harris J.R.: *Integration of spectral, thermal, and textural features of ASTER data using Random Forests classification for lithological mapping*. Journal of African Earth Sciences, vol. 129, 2017, pp. 445–457. <https://doi.org/10.1016/j.jafrearsci.2017.01.028>.
- [5] Serbouti I., Raji M., Hakdaoui M., Pradhan B., Lee C.-W., Alamri A.M.: *Pixel and object-based machine learning classification schemes for lithological mapping enhancement of Semi-Arid regions using Sentinel-2A imagery: A case study of the southern Moroccan Meseta*. IEEE Access, vol. 9, 2021, pp. 119262–119278. <https://doi.org/10.1109/ACCESS.2021.3107294>.
- [6] Shahin M.A., Jaksa M.B., Maier H.R.: *Artificial neural network applications in geotechnical engineering*. Australian Geomechanics, vol. 36(1), 2001, pp. 49–62.
- [7] Shahin M.A., Jaksa M.B.: *Neural network prediction of pullout capacity of marquee ground anchors*. Computers and Geotechnics, vol. 32(1), 2005, pp. 153–163. <https://doi.org/10.1016/j.compgeo.2005.02.003>.
- [8] Das S.K., Basudhar P.K.: *Prediction of residual friction angle of clays using artificial neural network*. Engineering Geology, vol. 100(3–4), 2008, pp. 142–145. <https://doi.org/10.1016/j.enggeo.2008.03.001>.
- [9] Azamathulla H.M., Guven A., Demir Y.K.: *Linear genetic programming to scour below submerged pipeline*. Ocean Engineering, vol. 38(8–9), 2011, pp. 995–1000. <https://doi.org/10.1016/j.oceaneng.2011.03.005>.
- [10] Garg A., Tai K., Gupta A.K.: *A modified multi-gene genetic programming approach for modelling true stress of dynamic strain aging regime of austenitic stainless steel 304*. Meccanica, vol. 49(5), 2014, pp. 1193–1209. <https://doi.org/10.1007/s11012-013-9873-x>.
- [11] Hajaj S., El Harti A., Jellouli A., Pour A.B., Mnissar Himyari S., Hamzaoui A., Hashim M.: *Evaluating the Performance of Machine Learning and Deep Learning Techniques to HyMap Imagery for Lithological Mapping in a Semi-Arid Region: Case Study from Western Anti-Atlas, Morocco*. Minerals, vol. 13(6), 2023, 766. <https://doi.org/10.3390/min13060766>.
- [12] El-Omairi M.A., El Garouani A.: *A review on advancements in lithological mapping utilizing machine learning algorithms and remote sensing data*. Heliyon, 2023, vol. 9(9), e20168. <https://doi.org/10.1016/j.heliyon.2023.e20168>.
- [13] Santos D., Cardoso-Fernandes J., Lima A., Müller A., Brönnner M., Teodoro A.C.: *Spectral analysis to improve inputs to random forest and other boosted ensemble tree-based algorithms for detecting NYF pegmatites in Tysfjord, Norway*. Remote Sensing, vol. 14(15), 2022, 3532. <https://doi.org/10.3390/rs14153532>.

- [14] Cardoso-Fernandes J., Teodoro A.C., Lima A., Roda-Robles E.: *Semi-automation of support vector machines to map lithium (Li) bearing pegmatites*. Remote Sensing, vol. 12(14), 2020, 2319. <https://doi.org/10.3390/rs12142319>.
- [15] Lary D.J., Alavi A.H., Gandomi A.H., Walker A.L.: *Machine learning in geosciences and remote sensing*. Geoscience Frontiers, vol. 7(1), 2016, pp. 3–10. <https://doi.org/10.1016/j.gsf.2015.07.003>.
- [16] Rowan L.C., Mars J.C.: *Lithologic mapping in the Mountain Pass, California area using advanced spaceborne thermal emission and reflection radiometer (ASTER) data*. Remote Sensing of Environment, vol. 84(3), 2003, pp. 350–366. [https://doi.org/10.1016/S0034-4257\(02\)00127-X](https://doi.org/10.1016/S0034-4257(02)00127-X).
- [17] Massironi M., Bertoldi L., Calafa P., Visonà D., Bistacchi A., Giardino C., Schiavo A.: *Interpretation and processing of ASTER data for geological mapping and granitoids detection in the Saghro massif (eastern Anti-Atlas, Morocco)*. Geosphere, vol. 4(4), 2008, pp. 736–759. <https://doi.org/10.1130/GES00161.1>.
- [18] Harvey A.S., Fotopoulos G.: *Geological mapping using machine learning algorithms*. The International Archives of the Photogrammetry, Remote Sensing and Spatial Information Sciences, vol. XLI-B8, 2016, pp. 423–430. <https://doi.org/10.5194/isprs-archives-XLI-B8-423-2016>.
- [19] Serbouti I., Raji M., Hakdaoui M., El Kamel F., Pradhan B., Gite S., Alamri A., Maulud K.N.A., Dikshit A.: *Improved lithological map of large complex Semi-Arid regions using spectral and textural datasets within Google Earth Engine and Fused Machine Learning Multi-Classifiers*. Remote Sensing, vol. 14(21), 2022, 5498. <https://doi.org/10.3390/rs14215498>.
- [20] Drury S.A.: *Image Interpretation in Geology*. Allen & Unwin, London 1987.
- [21] Ninomiya Y., Fu B., Cudahy T.J.: *Detecting lithology with Advanced Spaceborne Thermal Emission and Reflection Radiometer (ASTER) multispectral thermal infrared “radiance-at-sensor” data*. Remote Sensing of Environment, vol. 99(1–2), 2005, pp. 127–139. <https://doi.org/10.1016/j.rse.2005.06.009>.
- [22] Gad S., Kusky T.: *ASTER spectral ratioing for lithological mapping in the Arabian-Nubian shield, the Neoproterozoic Wadi Kid area, Sinai, Egypt*. Gondwana Research, vol. 11(3), 2007, pp. 326–335. <https://doi.org/10.1016/j.gr.2006.02.010>.
- [23] Leverington D.W., Moon W.M.: *Landsat-TM-based discrimination of lithological units associated with the Purtuniqu ophiolite, Quebec, Canada*. Remote Sensing, vol. 4(5), 2012, pp. 1208–1231. <https://doi.org/10.3390/rs4051208>.
- [24] Black M., Riley T.R., Ferrier G., Fleming A.H., Fretwell P.T.: *Automated lithological mapping using airborne hyperspectral thermal infrared data: A case study from Anchorage Island, Antarctica*. Remote Sensing of Environment, vol. 176, 2016, pp. 225–241. <https://doi.org/10.1016/j.rse.2016.01.022>.
- [25] Rowan L.C., Schmidt R.G., Mars J.C.: *Distribution of hydrothermally altered rocks in the Reko Diq, Pakistan mineralized area based on spectral analysis of ASTER data*. Remote Sensing of Environment, vol. 104(1), 2006, pp. 74–87. <https://doi.org/10.1016/j.rse.2006.05.014>.

- [26] Kratt C., Calvin W.M., Coolbaugh M.F.: *Mineral mapping in the Pyramid Lake basin: Hydrothermal alteration, chemical precipitates and geothermal energy potential*. Remote Sensing of Environment, vol. 114(10), 2010, pp. 2297–2304. <https://doi.org/10.1016/j.rse.2010.05.006>.
- [27] Zhang T., Yi G., Li H., Wang Z., Tang J., Zhong K., Li Y., Wang Q., Bie X.: *Integrating data of ASTER and Landsat-8 OLI (AO) for hydrothermal alteration mineral mapping in duolong porphyry cu-au deposit, Tibetan Plateau, China*. Remote Sensing, vol. 8(11), 2016, 890. <https://doi.org/10.3390/rs8110890>.
- [28] Vaughan R.G., Hook S.J., Calvin W.M., Tarantik J.V.: *Surface mineral mapping at Steamboat Springs, Nevada, USA, with multi-wavelength thermal infrared images*. Remote Sensing of Environment, vol. 99(1–2), 2005, pp. 140–158. <https://doi.org/10.1016/j.rse.2005.04.030>.
- [29] Vicente L.E., de Souza Filho C.R.: *Identification of mineral components in tropical soils using reflectance spectroscopy and advanced spaceborne thermal emission and reflection radiometer (ASTER) data*. Remote Sensing of Environment, vol. 115(8), 2011, pp. 1824–1836. <https://doi.org/10.1016/j.rse.2011.02.023>.
- [30] Govil H., Gill N., Rajendran S., Santosh M., Kumar S.: *Identification of new base metal mineralization in Kumaon Himalaya, India, using hyperspectral remote sensing and hydrothermal alteration*. Ore Geology Reviews, vol. 92, 2018, pp. 271–283. <https://doi.org/10.1016/j.oregeorev.2017.11.023>.
- [31] Gemusse U., Cardoso-Fernandes J., Lima A., Teodoro A.: *Identification of pegmatites zones in Muiane and Naipa (Mozambique) from Sentinel-2 images, using band combinations, band ratios, PCA and supervised classification*. Remote Sensing Applications: Society and Environment, vol. 32, 2023, 101022. <https://doi.org/10.1016/j.rsase.2023.101022>.
- [32] Tagwai M.G., Jimoh O.A., Shehu S.A., Zabidi H.: *Application of GIS and remote sensing in mineral exploration: current and future perspectives*. World Journal of Engineering, vol. 21(3), 2023, pp. 487–502. <https://doi.org/10.1108/WJE-09-2022-0395>.
- [33] Kruse F.A., Dietz J.B.: *Integration of diverse remote sensing data sets for geologic mapping and resource exploration*, [in:] Curran R.J., Smith J.A., Watson K. (eds.), *Earth and Atmospheric Remote Sensing: 2–4 April 1991 Orlando, Florida*, Proceedings of SPIE, vol. 1492, SPIE – The International Society for Optical Engineering, 1991, pp. 326–337. <https://doi.org/10.1117/12.45859>.
- [34] Al-Anazi A., Gates I.D.: *A support vector machine algorithm to classify lithofacies and model permeability in heterogeneous reservoirs*. Engineering Geology, vol. 114(3–4), 2010, pp. 267–277. <https://doi.org/10.1016/j.enggeo.2010.05.005>.
- [35] Sebtosheikh M.A., Salehi A.: *Lithology prediction by support vector classifiers using inverted seismic attributes data and petrophysical logs as a new approach and investigation of training data set size effect on its performance in a heterogeneous*

- carbonate reservoir*. Journal of Petroleum Science and Engineering, vol. 134, 2015, pp. 143–149. <https://doi.org/10.1016/j.petrol.2015.08.001>.
- [36] Deng C., Pan H., Fang S., Konaté A.A., Qin R.: *Support vector machine as an alternative method for lithology classification of crystalline rocks*. Journal of Geophysics and Engineering, vol. 14(2), 2017, pp. 341–349. <https://doi.org/10.1088/1742-2140/aa5b5b>.
- [37] Bhattacharya S., Carr T.R., Pal M.: *Comparison of supervised and unsupervised approaches for mudstone lithofacies classification: Case studies from the Bakken and Mahantango-Marcellus Shale, USA*. Journal of Natural Gas Science and Engineering, vol. 33, 2016, pp. 1119–1133. <https://doi.org/10.1016/j.jngse.2016.04.055>.
- [38] Xie Y., Zhu C., Zhou W., Li Z., Liu X., Tu M.: *Evaluation of machine learning methods for formation lithology identification: A comparison of tuning processes and model performances*. Journal of Petroleum Science and Engineering, vol. 160, 2018, pp. 182–193. <https://doi.org/10.1016/j.petrol.2017.10.028>.
- [39] Sun J., Li Q., Chen M., Ren L., Huang G., Li C., Zhang Z.: *Optimization of models for a rapid identification of lithology while drilling – a win-win strategy based on machine learning*. Journal of Petroleum Science and Engineering, vol. 176, 2019, pp. 321–341. <https://doi.org/10.1016/j.petrol.2019.01.006>.
- [40] Merembayev T., Yunussov R., Yedilkhan A.: *Machine learning algorithms for classification geology data from well logging*, [in:] 2018 14th International Conference on Electronics Computer and Computation (ICECCO), Kaskelen, Kazakhstan, 2018, IEEE, Piscataway 2018, pp. 206–212. <https://doi.org/10.1109/ICECCO.2018.8634775>.
- [41] Dev V.A., Eden M.R.: *Evaluating the boosting approach to machine learning for formation lithology classification*. Computer Aided Chemical Engineering, vol. 44, 2018, pp. 1465–1470. <https://doi.org/10.1016/B978-0-444-64241-7.50239-1>.
- [42] Dev V.A., Eden M.R.: *Formation lithology classification using scalable gradient boosted decision trees*. Computers & Chemical Engineering, vol. 128, 2019, pp. 392–404. <https://doi.org/10.1016/j.compchemeng.2019.06.001>.
- [43] Raeesi M., Moradzadeh A., Ardejani F.D., Rahimi M.: *Classification and identification of hydrocarbon reservoir lithofacies and their heterogeneity using seismic attributes, logs data and artificial neural networks*. Journal of Petroleum Science and Engineering, vol. 82–83, 2012, pp. 151–165. <https://doi.org/10.1016/j.petrol.2012.01.012>.
- [44] Ouadfeul S.-A., Aliouane L.: *Lithofacies classification using the multilayer perceptron and the self-organizing neural networks*, [in:] Huang T., Zeng Z., Li C., Leung C.S. (eds.), *Neural Information Processing: 19th International Conference, ICONIP 2012, Doha, Qatar, November 12–15, 2012, Proceedings, Part V*, Lecture Notes in Computer Science, vol. 7667, Springer, Berlin, Heidelberg 2012, pp. 737–744. https://doi.org/10.1007/978-3-642-34500-5_87.

- [45] Zych M., Stachura G., Hanus R., Szabó N.P.: *Application of artificial neural networks in identification of geological formations on the basis of well logging data – a comparison of computational environments' efficiency*, [in:] Hanus R., Mazur D., Kreisler C. (eds.), *Methods and Techniques of Signal Processing in Physical Measurements, MSM 2018*, Lecture Notes in Electrical Engineering, vol. 548, Springer, Cham 2019, pp. 416–422. https://doi.org/10.1007/978-3-030-11187-8_34.
- [46] Salehi S.M., Honarvar B.: *Automatic identification of formation lithology from well log data: a machine learning approach*. *Journal of Petroleum Science Research*, vol. 3(2), pp. 73–82, 2014.
- [47] Li Z., Kang Y., Feng D., Wang X.-M., Lv W., Chang J., Zheng W.X.: *Semi-supervised learning for lithology identification using Laplacian support vector machine*. *Journal of Petroleum Science and Engineering*, vol. 195, 2020, 107510. <https://doi.org/10.1016/j.petrol.2020.107510>.
- [48] Ikenne M., Mortaji A., Gasquet D., Stussi J.M.: *Les filons basiques des boutonnières du Bas Drâa et de la Tagragra d'Akka: Témoins des distensions néo-protérozoïques de l'Anti-Atlas occidental (Maroc)*. *Journal of African Earth Sciences*, vol. 25(2), 1997, pp. 209–223. [https://doi.org/10.1016/S0899-5362\(97\)00099-7](https://doi.org/10.1016/S0899-5362(97)00099-7).
- [49] Benbrahim M., Aissa M., Zouhair M.: *Synthèse géologique et métallogénique du gisement aurifère d'Iourirne (Boutonnière de Tagragra d'Akka, Anti-Atlas occidental, Maroc)*. *International Journal of Innovation and Applied Studies*, vol. 24(1), 2018, pp. 428–438.
- [50] Maacha L.: *Études métallogéniques et géophysiques des minéralisations cobaltifères et cuprifères de Bou-Azzer El Graara, Anti-Atlas Maroc*. Université Cadi Ayyad, Marrakech 2013 [Ph.D. thesis, unpublished].
- [51] Adiri Z., Lhissou R., Maacha L., Jilali A., Talbi E.H., Jellouli A., Chakouri M.: *Comparison of ASTER GDEM3, SRTM3, NASADEM, TanDEM-X90, AW3D30, and ALOS PALSAR data with TanDEM-X12: A case study of Tagragra of Akka inlier, Moroccan Anti-Atlas*. *Arabian Journal of Geosciences*, vol. 15(21), 2022, 1654. <https://doi.org/10.1007/s12517-022-10885-x>.
- [52] Zouhair M., Marignac C.: *Les paléocirculations fluides dans la Tagragra d'Akka (Anti-Atlas, Maroc): Etude combinée des inclusions fluides et de la déformation des quartz aurifères: conséquences pour la métallogénie de l'or*. Institut National Polytechnique de Lorraine, Nancy 1992 [Ph.D. thesis].
- [53] Benbrahim M., Aissa M.: *Le gisement aurifère d'Iourirn (boutonnière de Tagragra d'Akka, Anti-Atlas occidental, Maroc): Un exemple de minéralisation mésothermale dans les formations paléoprotérozoïques*. *Bulletin de l'Institut Scientifique*, no. 27, 2005, pp. 41–46.
- [54] Boya T.K.L.D.: *Pétrologie, métallogénie et géochimie des altérations hydrothermales des gisements aurifères d'Angarf, Irbiben et Ifarar (boutonnière Tagragra d'Akka, Anti-Atlas, Maroc)*. Université Ibn Tofail, Kénitra 2014 [Ph.D. thesis].

- [55] Potherat P., Ait Kassi M., Nicot P., Macaudiere J., Marignac C.: *Structural evolution of gold-bearing quartz veins in the Precambrian exposures of the Tagragra d'Akka (western Anti-Atlas, Morocco)*, [in:] Pagel M., Leroy J. (eds.), *Source, Transport and Deposition of Metals: Proceedings of the 25 Years SGA Anniversary Meeting, Nancy, 30 August–3 September, 1991*, Balkema, Rotterdam 1991, pp. 477–480.
- [56] Choubert G.: *Histoire géologique du Précambrien de l'Anti-Atlas. Tome 1*. Éditions du Service Géologique du Maroc, Rabat 1963.
- [57] Mortaji A.: *La boutonnière précambrienne de Tagragra d'Akka (Anti-Atlas occidental, Maroc): Pétrologie et géochimie des granitoïdes, filons basiques et métamorphites associées*. l'Université Henri Poincaré, Nancy 1989 [Ph.D. thesis].
- [58] Michard A.: *Éléments de Géologie Marocaine*. Éditions du Service Géologique du Maroc, Rabat 1976.
- [59] Hassenforder B., Roger J., Baudin T., Chalot-Prat F., Gasquet D., Berrahma A., Chèvremont P., Marquer D., Razin P., Benlakhdim: *Carte géologique de Sidi Bou'addi (Maroc) au 1/50 000, avec notice explicative*. Notes et Mémoires du Service Géologique, no. 414, Editions du Service Géologique du Maroc, Rabat 2001.
- [60] Roger J., Gasquet D., Baudin T., Chalot-Prat F., Hassenforder B., Marquer I.D., Chèvremont P., Berrahma A., Destombes J., Razin P., Benlakhdim A.: *Carte géologique de Tamazrar (Maroc) à 1/50 000, avec notice explicative*. Notes et Mémoires du Service Géologique, no. 415, Editions du Service Géologique du Maroc, Rabat 2001.
- [61] Gasquet D., Chevremont P., Baudin T., Chalot-Prat F., Guerrot C., Cocherie A., Roger J., Hassenforder B., Cheilletz A.: *Polycyclic magmatism in the Tagragra d'Akka and Kerdous-Tafeltast inliers (Western Anti-Atlas, Morocco)*. *Journal of African Earth Sciences*, vol. 39(3–5), 2004, pp. 267–275. <https://doi.org/10.1016/j.jafrearsci.2004.07.062>.
- [62] Boya T.K.L.-D., Gnanzou A., Hervé K.J.L., Adingra P.K.M., Goulihi D.D., M'Rabet S.: *Petrography and geochemistry for proposal of geodynamic model for the Irbiben granite in Tagragra d'Akka inlier, (western Anti-Atlas, Morocco)*. *Journal of Geoscience, Engineering, Environment, and Technology*, vol. 7(3), 2022, pp. 102–109. <https://doi.org/10.25299/jgeet.2022.7.3.10275>.
- [63] Hassenforder B.: *La tectonique panafricaine et varisque de l'Anti-Atlas dans le massif du Kerdous (Maroc)*. Université Louis Pasteur, Strasbourg 1987 [Ph.D. thesis].
- [64] Marignac C.: *Contribution à l'étude du potentiel aurifère des Tagragra d'Akka et de Tata*. Rapport inédit, BRPM, Rabat 1990.
- [65] ESA Sentinel-2 Team: *GMES Sentinel-2 mission requirements document*. European Space Agency, 2007. <https://citeseerx.ist.psu.edu/document?repid=rep1&type=pdf&doi=0f3f3987fa4ec266f76efbe180b1ebb9129a4dc8> [access: 5.10.2024].
- [66] European Space Agency: *ALOS PRISM L1B, Version 1.0*. <https://earth.esa.int/eogateway/catalog/alos-prism-l1b> [access: 3.02.2024].

- [67] Ozendi M., Topan H., Cam A., Bayık Ç.: *Pan sharpening quality investigation of Turkish in-operation remote sensing satellites: Applications with RASAT and GÖKTÜRK-2 images*. The International Archives of the Photogrammetry, Remote Sensing and Spatial Information Sciences, vol. XLII-2/W1, 2016, pp. 131–135. <https://doi.org/10.5194/isprs-archives-XLII-2-W1-131-2016>.
- [68] Kaplan G.: *Sentinel-2 pan sharpening – comparative analysis*. Proceedings, vol. 2(7), 2018, 345. <https://doi.org/10.3390/eocrs-2-05158>.
- [69] Pohl C., van Genderen J.L.: *Multisensor fusion: optimization and operationalization for mapping applications*, [in:] Kadar I., Libby V. (eds.), *Signal Processing, Sensor Fusion, and Target Recognition III: 4–8 April 1994, Orlando, Florida, United States*, Proceedings of SPIE, vol. 2232, SPIE – The International Society for Optical Engineering, 1994, pp. 12–25. <https://doi.org/10.1117/12.177750>.
- [70] Sheffield C.: *Selecting band combinations from multi spectral data*. Photogrammetric Engineering and Remote Sensing, vol. 51(6), 1985, pp. 681–687.
- [71] Pohl C., van Genderen J.L.: *Review article. Multisensor image fusion in remote sensing: Concepts, methods and applications*. International Journal of Remote Sensing, vol. 19(5), 1998, pp. 823–854. <https://doi.org/10.1080/014311698215748>.
- [72] Bakioğlu O.B., Topan H., Özendi M., Cam A.: *Pan sharpening of RASAT and GÖKTÜRK-2 images via high pass filter*. The International Archives of the Photogrammetry, Remote Sensing and Spatial Information Sciences, vol. XLII-4/W6, 2017, pp. 27–29. <https://doi.org/10.5194/isprs-archives-XLII-4-W6-27-2017>.
- [73] Vrabel J., Doraiswamy P., Stern A.: *Application of hyperspectral imagery resolution improvement for site-specific farming*, [in:] XXII FIG International Congress: ACSM-ASPRS Conference and Technology Exhibition 2002 congress/conference proceedings: April 19–26, 2002, Washington, D.C., American Society for Photogrammetry and Remote Sensing, Washington 2002.
- [74] Vrabel J.C., Doraiswamy P., McMurtrey James E. III, Stern A.: *Demonstration of the accuracy of improved-resolution hyperspectral imagery*, [in:] Shen S.S., Lewis P.E. (eds.), *Algorithms and Technologies for Multispectral, Hyperspectral, and Ultraspectral Imagery VIII: 23–27 April 2012, Baltimore, Maryland, United States*, Proceedings of SPIE, vol. 4725, SPIE – The International Society for Optical Engineering, 2002, pp. 556–567. <https://doi.org/10.1117/12.478790>.
- [75] Despini F., Teggi S., Baraldi A.: *Methods and metrics for the assessment of pan-sharpening algorithms*, [in:] Bruzzone L. (ed.), *Image and Signal Processing for Remote Sensing XX: 22–24 September 2014, Amsterdam, Netherlands*, Proceedings of SPIE, vol. 9244, SPIE – The International Society for Optical Engineering, 2014. <https://doi.org/10.1117/12.2067316>.
- [76] Gupta R.P.: *Remote Sensing Geology*. 3rd ed., Springer, Berlin, Heidelberg 2018. <https://doi.org/10.1007/978-3-662-55876-8>.
- [77] Jolliffe I.T., Cadima J.: *Principal component analysis: a review and recent developments*. Philosophical Transactions of the Royal Society A: Mathematical,

- Physical and Engineering Sciences, vol. 374(2065), 2016, 20150202. <https://doi.org/10.1098/rsta.2015.0202>.
- [78] Fung T., LeDrew E.: *Application of principal components analysis to change detection*. Photogrammetric Engineering and Remote Sensing, vol. 53(12), 1987, pp. 1649–1658.
- [79] Ready P., Wintz P.: *Information extraction, SNR improvement, and data compression in multispectral imagery*. IEEE Transactions on Communications, vol. 21(10), 1973, pp. 1123–1131. <https://doi.org/10.1109/TCOM.1973.1091550>.
- [80] Palaniswami C., Upadhyay A.K., Maheswarappa H.P.: *Spectral mixture analysis for subpixel classification of coconut*. Current Science, vol. 91(12), 2006, pp. 1706–1711. <http://www.jstor.org/stable/24094026>.
- [81] Conrad O., Bechtel B., Bock M., Dietrich H., Fischer E., Gerlitz L., Wehberg J., Wichmann V., Böhner J.: *System for Automated Geoscientific Analyses (SAGA) v. 2.1.4*. Geoscientific Model Development, vol. 8(7), 2015, pp. 1991–2007. <https://doi.org/10.5194/gmd-8-1991-2015>.
- [82] Dubey S.K., Vijay S., Pratibha: *A review of image segmentation using clustering methods*. International Journal of Applied Engineering Research, vol. 13(5), 2018, pp. 2484–2489.
- [83] Chen Z., Qi Z., Meng F., Cui L., Shi Y.: *Image segmentation via improving clustering algorithms with density and distance*. Procedia Computer Science, vol. 55, 2015, pp. 1015–1022. <https://doi.org/10.1016/j.procs.2015.07.096>.
- [84] Pal N.R., Pal S.K.: *A review on image segmentation techniques*. Pattern Recognition, vol. 26(9), 1993, pp. 1277–1294. [https://doi.org/10.1016/0031-3203\(93\)90135-J](https://doi.org/10.1016/0031-3203(93)90135-J).
- [85] Fukunaga K., Hostetler L.: *The estimation of the gradient of a density function, with applications in pattern recognition*. IEEE Transactions on Information Theory, vol. 21(1), 1975, pp. 32–40. <https://doi.org/10.1109/TIT.1975.1055330>.
- [86] Cheng Y.: *Mean shift, mode seeking, and clustering*. IEEE Transactions on Pattern Analysis and Machine Intelligence, vol. 17(8), 1995, pp. 790–799. <https://doi.org/10.1109/34.400568>.
- [87] Fei W., Zhu S.: *Mean shift clustering-based moving object segmentation in the H.264 compressed domain*. IET Image Processing, vol. 4(1), 2010, pp. 11–18. <https://doi.org/10.1049/iet-ipr.2009.0038>.
- [88] Liu C., Zhou A., Zhang Q., Zhang G.: *Adaptive image segmentation by using mean-shift and evolutionary optimisation*. IET Image Processing, vol. 8(6), 2014, pp. 327–333. <https://doi.org/10.1049/iet-ipr.2013.0195>.
- [89] Soysal Ö.M., Schneider H., Shrestha A., Guempel C.D., Li P., Donepudi H., Kondoju N.K., Sekeroglu K.: *Zonal statistics to identify hot-regions of traffic accidents*, [in:] Arabnia H.R., Deligiannidis L., Marsh A., Solo A.M..G. (eds.), *Proceedings of the 2012 International Conference on Modeling, Simulation & Visualization Methods MSV 2012: WORLDCOMP'12, July 16–19, 2012, Las Vegas, Nevada, USA*, pp. 287–293. <http://worldcomp-proceedings.com/proc/p2012/MSV6182.pdf> [access: 23.02.2024].

- [90] Jog S., Dixit M.: *Supervised classification of satellite images*, [in:] *2016 Conference on Advances in Signal Processing (CASP), Pune, India*, IEEE, Piscataway 2016, pp. 93–98. <https://doi.org/10.1109/CASP.2016.7746144>.
- [91] Perumal K., Bhaskaran R.: *Supervised classification performance of multispectral images*. *Journal of Computing*, vol. 2(2), 2010, pp. 124–129. <https://doi.org/10.48550/arXiv.1002.4046>.
- [92] Bachri I., Hakdaoui M., Raji M., Teodoro A.C., Benbouziane A.: *Machine learning algorithms for automatic lithological mapping using remote sensing data: A case study from Souk Arbaa Sahel, Sidi Ifni Inlier, Western Anti-Atlas, Morocco*. *ISPRS International Journal of Geo-Information*, vol. 8(6), 2019, 248. <https://doi.org/10.3390/ijgi8060248>.
- [93] European Space Agency: *Sentinel Application Platform (SNAP)*. Paris, 2023. <https://earth.esa.int/eogateway/tools/snap>.
- [94] Xavier Pons J.C., Sanjurjo-Vílchez J.: *Some notes on the divergence and transformed divergence formulae in the remote sensing literature*. *Remote Sensing Letters*, vol. 15(11), 2024, pp. 1187–1194. <https://doi.org/10.1080/2150704X.2024.2420286>.
- [95] Gholamy A., Kreinovich V., Kosheleva O.: *Why 70/30 or 80/20 relation between training and testing sets: A pedagogical explanation*. *International Journal of Intelligent Technologies and Applied Statistics*, vol. 11(2), 2018, pp. 105–111. [https://doi.org/10.6148/IJITAS.201806_11\(2\).0003](https://doi.org/10.6148/IJITAS.201806_11(2).0003).
- [96] Vapnik V.: *The Nature of Statistical Learning Theory*. Springer, New York 1995.
- [97] Grizonnet M., Michel J., Poughon V., Inglada J., Savinaud M., Cresson R.: *Orfeo ToolBox: Open source processing of remote sensing images*. *Open Geospatial Data, Software and Standards*, vol. 2, 2017, 15. <https://doi.org/10.1186/s40965-017-0031-6>.
- [98] Luque A., Carrasco A., Martín A., de las Heras A.: *The impact of class imbalance in classification performance metrics based on the binary confusion matrix*. *Pattern Recognition*, vol. 91, 2019, pp. 216–231. <https://doi.org/10.1016/j.pat-cog.2019.02.023>.
- [99] Grandini M., Bagli E., Visani G.: *Metrics for multi-class classification: An overview*. arXiv preprint arXiv:2008.05756, 2020. <https://doi.org/10.48550/arXiv.2008.05756>.
- [100] Landis J.R., Koch G.G.: *The measurement of observer agreement for categorical data*. *Biometrics*, vol. 33(1), 1977, pp. 159–174. <https://doi.org/10.2307/2529310>.
- [101] Zengeya F.M., Mutanga O., Murwira A.: *Linking remotely sensed forage quality estimates from WorldView-2 multispectral data with cattle distribution in a savanna landscape*. *International Journal of Applied Earth Observation and Geoinformation*, vol. 21, 2013, pp. 513–524. <https://doi.org/10.1016/j.jag.2012.07.008>.
- [102] Chen Y., Wang Y., Zhang F., Dong Y., Song Z., Liu G.: *Remote sensing for lithology mapping in vegetation-covered regions: Methods, challenges, and opportunities*. *Minerals*, vol. 13(9), 2023, 1153. <https://doi.org/10.3390/min13091153>.

-
- [103] Dong Y., Yang Z., Liu Q., Zuo R., Wang Z.: *Fusion of GaoFen-5 and Sentinel-2B data for lithological mapping using vision transformer dynamic graph convolutional network*. *International Journal of Applied Earth Observation and Geoinformation*, vol. 129, 2024, 103780. <https://doi.org/10.1016/j.jag.2024.103780>.
- [104] Karimzadeh S., Tangestani M.H.: *Evaluating the VNIR-SWIR datasets of WorldView-3 for lithological mapping of a metamorphic-igneous terrain using support vector machine algorithm; a case study of Central Iran*. *Advances in Space Research*, vol. 68(6), 2021, pp. 2421–2440. <https://doi.org/10.1016/j.asr.2021.05.002>.
- [105] Ye B., Tian S., Ge J., Sun Y.: *Assessment of WorldView-3 data for lithological mapping*. *Remote Sensing*, vol. 9(11), 2017, 1132. <https://doi.org/10.3390/rs9111132>.
- [106] El-Omairi M.A., Garouani A.E.: *A review on advancements in lithological mapping utilizing machine learning algorithms and remote sensing data*. *Heliyon*, vol. 9(9), 2023, e20168. <https://doi.org/10.1016/j.heliyon.2023.e20168>.